Table 2. Eighty-eight genes composing the progression-free survival-related profile.

GenBank Acc.	GeneSymbol	Cytoband	β_{ridge}[a]	Description
NM_001123	*ADK*	10q22.2	0.006	adenosine kinase
NM_006408	*AGR2*	7p21.1	0.128	anterior gradient homolog 2 (Xenopus laevis)
NM_080429	*AQP10*	1q21.3	−0.162	aquaporin 10
NM_001040118	*ARAP1*	11q13.4	0.141	ArfGAP with RhoGAP domain, ankyrin repeat and PH domain 1
NM_006420	*ARFGEF2*	20q13.13	0.032	ADP-ribosylation factor guanine nucleotide-exchange factor 2 (brefeldin A-inhibited)
NM_181575	*AUP1*	2p13.1	0.129	ancient ubiquitous protein 1
NM_004776	*B4GALT5*	20q13.13	0.215	UDP-Gal:betaGlcNAc beta 1,4- galactosyltransferase, polypeptide 5
NM_138639	*BCL2L12*	19q13.33	−0.189	BCL2-like 12 (proline rich)
NM_020643	*C11orf16*	11p15.4	0.221	chromosome 11 open reading frame 16
NM_145061	*C13orf3*	13q12.11	−0.107	chromosome 13 open reading frame 3
NM_024032	*C17orf53*	17q21.31	−0.184	chromosome 17 open reading frame 53
NM_001144956	*C1orf230*	1q21.3	0.012	chromosome 1 open reading frame 230
NM_022106	*C20orf177*	20q13.33	0.167	chromosome 20 open reading frame 177
NM_000715	*C4BPA*	1q32.2	−0.505	complement component 4 binding protein, alpha
NM_012337	*CCDC19*	1q23.2	−0.162	coiled-coil domain containing 19
NM_015603	*CCDC9*	19q13.32	0.263	coiled-coil domain containing 9
NM_005408	*CCL13*	17q12	−0.228	chemokine (C-C motif) ligand 13
NM_001252	*CD70*	19p13.3	−0.204	CD70 molecule
NM_078481	*CD97*	19p13.12	−0.137	CD97 molecule
NM_006383	*CIB2*	15q25.1	0.359	calcium and integrin binding family member 2
NM_182848	*CLDN10*	13q32.1	−0.292	claudin 10
NM_001316	*CSE1L*	20q13.13	−0.220	CSE1 chromosome segregation 1-like (yeast)
NM_024295	*DERL1*	8q24.13	0.007	Der1-like domain family, member 1
NM_001042517	*DIAPH3*	13q21.2	0.022	diaphanous homolog 3 (Drosophila)
NM_021120	*DLG3*	Xq13.1	−0.039	discs, large homolog 3 (Drosophila)
NM_020877	*DNAH2*	17p13.1	−0.378	dynein, axonemal, heavy chain 2
NM_018897	*DNAH7*	2q32.3	0.226	dynein, axonemal, heavy chain 7
NM_001394	*DUSP4*	8p21.1	0.007	dual specificity phosphatase 4
NM_004091	*E2F2*	1p36.12	0.220	E2F transcription factor 2
NM_006795	*EHD1*	11q13.1	0.248	EH-domain containing 1
NM_020819	*FAM135A*	6q13	0.142	family with sequence similarity 135, member A
NM_032181	*FAM176A*	2p12	−0.096	family with sequence similarity 176, member A
NM_015687	*FILIP1*	6q14.1	−0.188	filamin A interacting protein 1
NM_021784	*FOXA2*	20p11.21	0.184	forkhead box A2
NM_001454	*FOXJ1*	17q25.1	−0.344	forkhead box J1
NM_000819	*GART*	21q22.11	0.140	phosphoribosylglycinamide formyltransferase, phosphoribosylglycinamide synthetase, phosphoribosylaminoimidazole synthetase
NM_178172	*GPIHBP1*	8q24.3	0.147	glycosylphosphatidylinositol anchored high density lipoprotein binding protein 1
NM_000189	*HK2*	2p13.1	−0.087	hexokinase 2
NM_002118	*HLA-DMB*	6p21.32	−0.288	major histocompatibility complex, class II, DM beta
NM_022465	*IKZF4*	12q13.2	−0.092	IKAROS family zinc finger 4 (Eos)
NM_016584	*IL23A*	12q13.2	0.493	interleukin 23, alpha subunit p19
NM_006801	*KDELR1*	19q13.32	−0.001	KDEL (Lys-Asp-Glu-Leu) endoplasmic reticulum protein retention receptor 1
NM_014895	*KIAA1009*	6q14.3	−0.150	KIAA1009
NM_017527	*LY6K*	8q24.3	0.226	lymphocyte antigen 6 complex, locus K
NM_005906	*MAK*	6p24.2	0.271	male germ cell-associated kinase
NM_024871	*MAP6D1*	3q27.1	−0.038	MAP6 domain containing 1
NM_031417	*MARK4*	19q13.32	0.040	MAP/microtubule affinity-regulating kinase 4
NM_024298	*MBOAT7*	19q13.42	−0.058	membrane bound O-acyltransferase domain containing 7
NM_002421	*MMP1*	11q22.2	−0.336	matrix metallopeptidase 1 (interstitial collagenase)
NM_181526	*MYL9*	20q11.23	0.058	myosin, light chain 9, regulatory

Table 2. Cont.

GenBank Acc.	GeneSymbol	Cytoband	β_{ridge}[a]	Description
NM_032344	*NUDT22*	11q13.1	0.198	nudix (nucleoside diphosphate linked moiety X)-type motif 22
NM_007224	*NXPH4*	12q13.3	−0.310	neurexophilin 4
NM_015311	*OBSL1*	2q35	−0.045	obscurin-like 1
NM_014982	*PCNX*	14q24.2	−0.098	pecanex homolog (Drosophila)
NM_014317	*PDSS1*	10p12.1	0.001	prenyl (decaprenyl) diphosphate synthase, subunit 1
NM_024420	*PLA2G4A*	1q31.1	0.107	phospholipase A2, group IVA (cytosolic, calcium-dependent)
NM_016341	*PLCE1*	10q23.33	0.029	phospholipase C, epsilon 1
NM_001031745	*RIBC1*	Xp11.22	0.209	RIB43A domain with coiled-coils 1
NM_015653	*RIBC2*	22q13.31	0.053	RIB43A domain with coiled-coils 2
NM_006987	*RPH3AL*	17p13.3	−0.043	rabphilin 3A-like (without C2 domains)
NM_001025070	*RPS14*	5q33.1	0.013	ribosomal protein S14
NM_152732	*RSPH9*	6p21.1	−0.102	radial spoke head 9 homolog (Chlamydomonas)
NM_014433	*RTDR1*	22q11.22	0.034	rhabdoid tumor deletion region gene 1
NM_005500	*SAE1*	19q13.32	0.038	SUMO1 activating enzyme subunit 1
NM_020150	*SAR1A*	10q22.1	0.277	SAR1 homolog A (S. cerevisiae)
NM_031469	*SH3BGRL2*	6q14.1	−0.281	SH3 domain binding glutamic acid-rich protein like 2
NM_003951	*SLC25A14*	Xq25	−0.344	solute carrier family 25 (mitochondrial carrier, brain), member 14
NM_014585	*SLC40A1*	2q32.2	0.065	solute carrier family 40 (iron-regulated transporter), member 1
NM_052910	*SLITRK1*	13q31.1	−0.314	SLIT and NTRK-like family, member 1
NM_172312	*SPAG8*	9p13.3	−0.123	sperm associated antigen 8
NM_145263	*SPATA18*	4q12	0.041	spermatogenesis associated 18 homolog (rat)
NM_006100	*ST3GAL6*	3q12.1	−0.192	ST3 beta-galactoside alpha-2,3-sialyltransferase 6
NM_018414	*ST6GALNAC1*	17q25.1	−0.175	ST6 (alpha-N-acetyl-neuraminyl-2,3-beta-galactosyl-1,3) -N-acetylgalactosaminide alpha-2,6-sialyltransferase 1
NM_032872	*SYTL1*	1p36.11	−0.084	synaptotagmin-like 1
NM_014466	*TEKT2*	1p34.3	−0.226	tektin 2 (testicular)
NM_005424	*TIE1*	1p34.2	0.250	tyrosine kinase with immunoglobulin-like and EGF-like domains 1
NM_198276	*TMEM17*	2p15	0.025	transmembrane protein 17
NM_199203	*TMEM189 -UBE2V1*	20q13.13	0.174	TMEM189-UBE2V1 readthrough transcript
NM_033550	*TP53RK*	20q13.12	0.054	TP53 regulating kinase
NM_139075	*TPCN2*	11q13.2	0.034	two pore segment channel 2
NM_018430	*TSNAXIP1*	16q22.1	0.170	translin-associated factor X interacting protein 1
NM_014023	*WDR37*	10p15.3	0.296	WD repeat domain 37
NM_018053	*XKR8*	1p35.3	0.106	XK, Kell blood group complex subunit-related family, member 8
NM_015896	*ZMYND10*	3p21.31	0.052	zinc finger, MYND-type containing 10
NM_005773	*ZNF256*	19q13.43	0.048	zinc finger protein 256
NM_024691	*ZNF419*	19q13.43	−0.042	zinc finger protein 419
NM_021089	*ZNF8*	19q13.43	0.093	zinc finger protein 8
NM_017975	*ZWILCH*	15q22.31	−0.074	Zwilch, kinetochore associated, homolog (Drosophila)

[a]A regression coefficient of each gene in ridge regression extension of multivariate Cox hazard model.

doi:10.1371/journal.pone.0009615.t002

was significantly correlated with overall survival time in multivariate analysis (HR, 1.51; 95% CI, 1.19–1.93, $p = 0.0008$).

Characterization of PFS-Related Profile

We conducted GO analysis to understand the biological characteristics of 88 PFS-related genes. To characterize the gene list based on GO classification on 'biological process', 'molecular function', and 'cellular component', we examined which categories were highly associated with the 88 genes. After multiple testing corrections using the FDR method [26], 8 categories were significantly overrepresented (FDR q-value<0.10) (Figure 4). In the 88 PFS-related genes, genes involved in GTPase binding (GO17016, GO31267 and GO51020), cellular localization (GO51649 and GO51641), intracellular transport (GO46907 and GO6886), and/or ciliary or flagellar motility (GO1539) were notably enriched. We investigated similarities in overrepresented GO categories between our 88 PFS-related genes and the previously reported gene expression profiles which were correlated to prognosis in ovarian cancer [11,13]. However, we could not identify common GO categories between our profile and the previously reported profiles (data not shown).

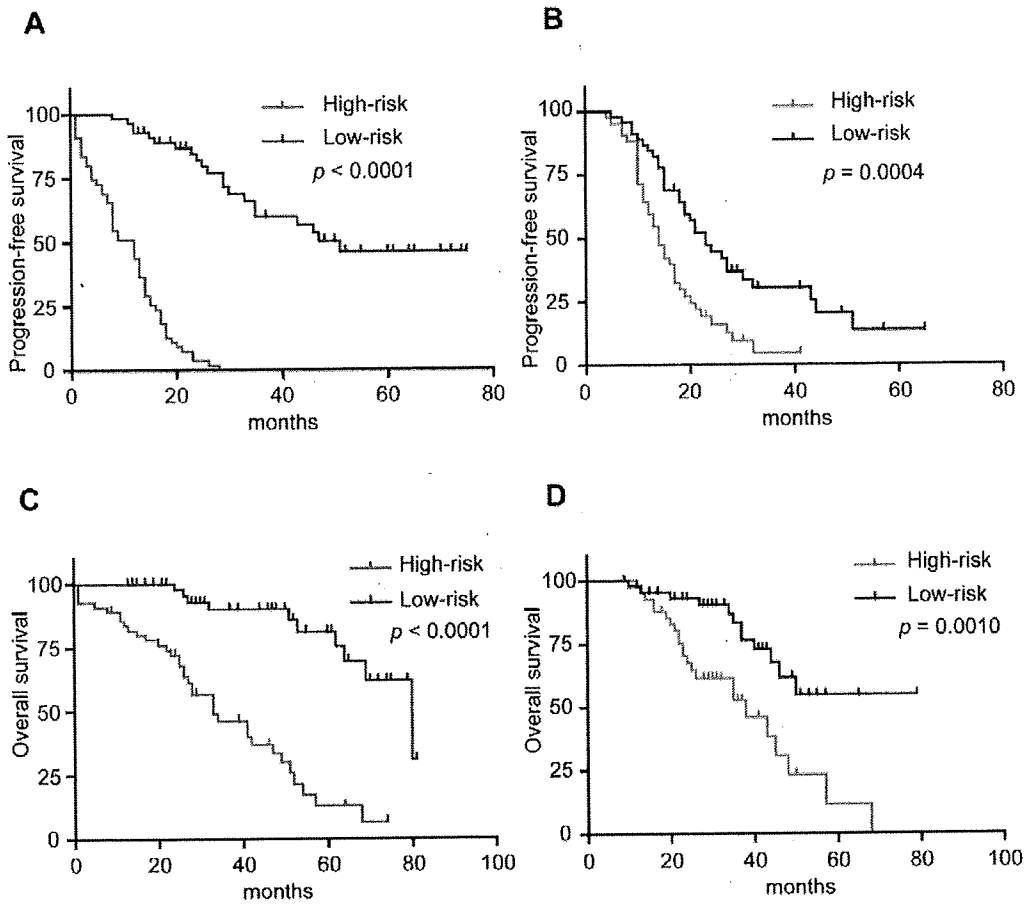

Figure 1. Prediction of prognosis in high-risk and low-risk patients based on the prognostic index. High-risk patients had significantly short progression-free survival times compared to low-risk patients (A) in the discovery set (log rank test, $p<0.0001$) and (B) in the external set (log rank test, $p=0.0004$). Similarly, high-risk patients had significantly shorter overall survival times compared to low-risk patients (C) in the discovery set (log rank test, $p<0.0001$) and (D) in the external set (log rank test, $p=0.0010$).
doi:10.1371/journal.pone.0009615.g001

We further used IPA software to analyze 88 PFS-related genes from the viewpoint of molecular interaction or pathway. Top three significant networks (score>25) are shown in Figures S5-7. The network 1 included 15 of the 88 prognostic genes, and was significantly associated with IPA-defined several networks: cell death, neurological disease, and cellular assembly and organization (Figure S5). Fourteen prognostic genes were included in the network 2, which was defined as networks related to cancer, cell morphology, and renal and urological disease (Figure S6). The network 3 displayed significant interactions and interrelations between genes involved in cell-to-cell signaling and interaction, hematological system development and function, and immune cell trafficking (Figure S7). In the 88 genes, we found several genes interacting with *SRC* or *MYC* (Figure S6), each of which was reported as a representative gene in oncogenic pathways of ovarian cancer [25,27].

Discussion

In this study, we identified the prognostic index for predicting PFS time in patients with advanced-stage serous ovarian cancer treated with platinum/taxane-based adjuvant chemotherapy across two types of microarray expression data from the present discovery set and publicly available external set by using the ridge regression Cox model. The significant correlation between our prognostic index and OS time was also indicated in the two independent datasets.

In expression microarray analysis, there is a so-called "curse of dimensionality" problem that the number of genes is much larger than the number of samples. To improve the reliability of a gene expression-based prognostic model, it is necessary to avoid overfitting to the dataset, and to confirm the reproducibility of the predictive ability in external independent datasets [28]. Until now, several bioinformatics approaches have been proposed to establish a model for survival prediction using microarray data [18,29]. Bøvelstad *et al.* [18] recently examined the prediction performance of the following seven methods: univariate selection, forward stepwise selection, principal components regression, supervised principal components regression, partial least squares regression, ridge regression and the lasso using three microarray datasets [Dutch breast cancer data (n = 295), diffuse large B-cell lymphoma data (n = 240), and Norway/Stanford breast cancer data (n = 115)] [7,30–32]. They concluded that the univariate Cox model alone was insufficient for predicting survival and that the ridge regression

Table 3. Univariate and multivariate Cox's proportional hazard model analysis of prognostic factors for progression-free survival.

	Univariate analysis		Multivariate analysis	
Prognostic factor	**Hazard ratio (95%CI*)**	***p*-value**	**Hazard ratio (95%CI)**	***p*-value**
A) Present study (n = 110)				
Age	0.99 (0.97–1.01)	0.41	1.00 (0.99–1.02)	0.68
Stage IV (vs Stage III)	1.40 (1.05–1.81)	0.022	0.93 (0.69–1.24)	0.65
Optimal Surgery (vs not optimal)	0.57 (0.45–0.72)	<0.0001	0.73 (0.56–0.94)	0.016
Grade				
Grade2 (vs Grade1)	1.21 (0.89–1.67)	0.23	1.08 (0.78–1.50)	0.66
Grade3 (vs Grade1)	1.44 (1.07–1.98)	0.016	1.34 (0.98–1.88)	0.065
Prognostic Index				
High (vs Low)	3.95 (2.85–5.74)	<0.0001	3.80 (2.68–5.61)	<0.0001
B) Tothill's dataset [20] (n = 87)				
Age	1.01 (0.98–1.03)	0.61	1.00 (0.98–1.03)	0.82
Stage IV (vs Stage III)	1.26 (0.51–2.28)	0.55	0.83 (0.33–1.55)	0.60
Optimal Surgery (vs not optimal)	0.78 (0.62–0.99)	0.049	0.76 (0.60–0.98)	0.035
Prognostic Index				
High (vs Low)	1.62 (1.26–2.09)	0.0001	1.64 (1.27–2.13)	0.0001

*CI denotes confidence interval.

doi:10.1371/journal.pone.0009615.t003

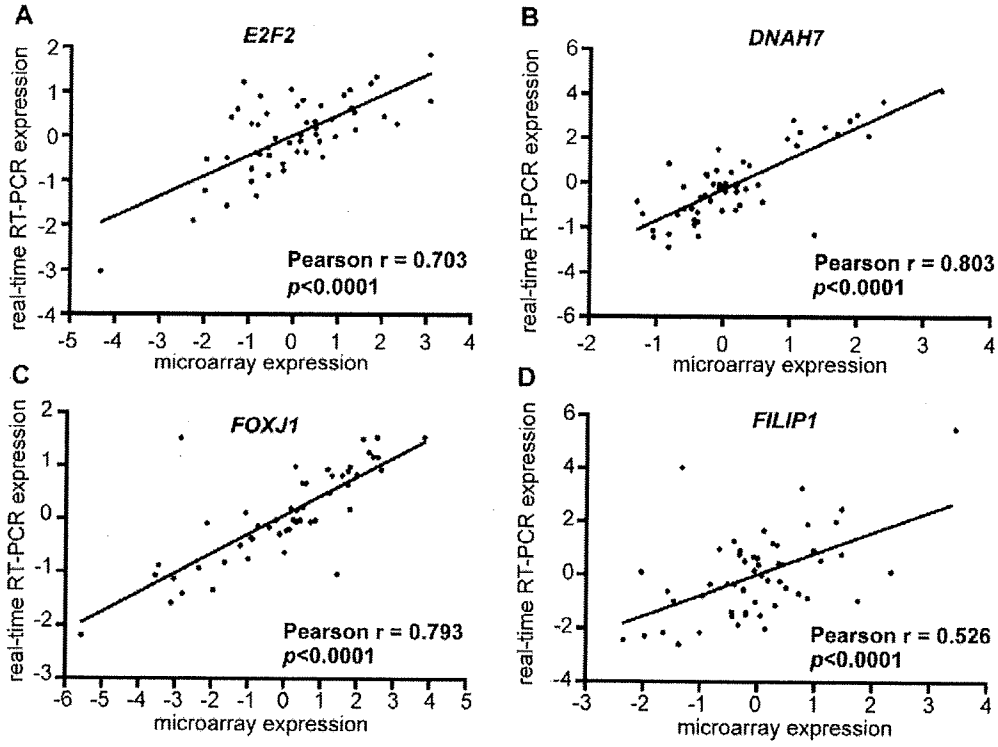

Figure 2. Validation of microarray expression data using quantitative real-time reverse transcript polymerase chain reaction (RT-PCR) analysis. There were significant correlations between microarray expression and real-time RT-PCR expression in (A) *E2F2*, (B) *DNAH7*, (C) *FOXJ1*, and (D) *FILIP1*.

doi:10.1371/journal.pone.0009615.g002

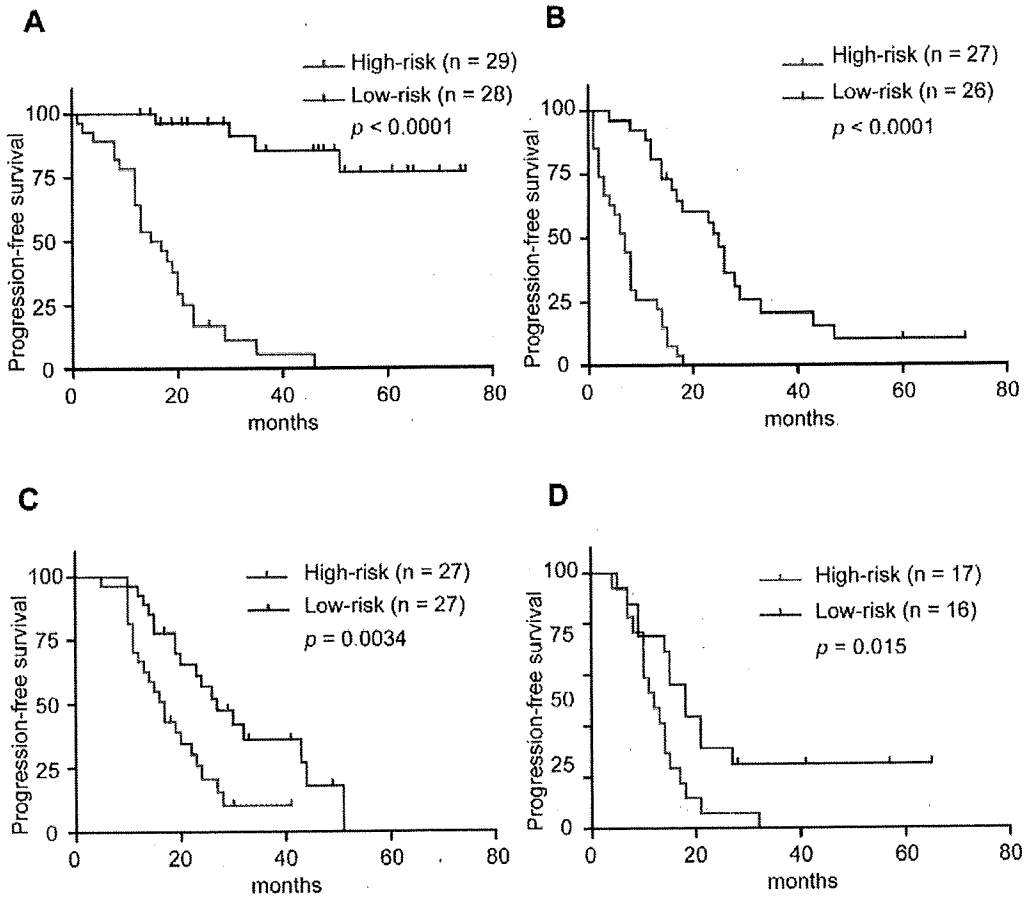

Figure 3. Prediction of prognosis in high-risk and low-risk patients based on the prognostic index after the stratification of patients according to the status of debulking surgery. High-risk patients had significantly short progression-free survival times compared to low-risk patients (A) in optimal (log rank test, $p<0.0001$) and (B) suboptimal group of discovery dataset (log rank test, $p<0.0001$). Similarly, high-risk patients had significantly shorter overall survival times compared to low-risk patients (C) in optimal (log rank test, $p=0.0034$) and (D) suboptimal group of the external dataset (log rank test, $p=0.015$).
doi:10.1371/journal.pone.0009615.g003

Cox model demonstrated the best performance in three datasets. Therefore, we used univariate Cox model only for selecting genes related to PFS time, and adjusted the regression coefficients by the ridge regression Cox model in order to increase the predictive performance of the prognostic index in our dataset.

The current study is intended to identify gene expression profile with a superior ability to predict prognosis than other clinicopathological factors. The stratification of patients with ovarian cancer according to clinicopathological prognostic factors is one of important analysis methods for the identification of highly accurate prognostic index [11]. After we stratified patients according to grade, FIGO stage, and status of debulking surgery, we investigated gene expression profile for predicting PFS time in stage III grade 2/3 serous ovarian cancer patients received optimal surgery or suboptimal surgery. However, we could find poorer predictive performance of the prognostic indices from the stratified analyses than that from the non-stratified analysis (Table S3). Besides the reduction of sample size in the discovery and external datasets after the stratification, a variety in clinical features and grading systems between the two datasets (Table S1) might influence the results from these stratified analyses. This is the main reason why we planned to identify prognostic index based on PFS-related genes in 110 advanced-stage serous ovarian cancers and then evaluate the significance of the prognostic index using multivariate analysis including grade, stage, and status of debulking surgery.

Although we enrolled ovarian cancer patients screened carefully by the following three categories: advanced-stage, histological serous-type, and platinum/taxane-based chemotherapy after primary surgery, we established no inclusion or exclusion criterion of histological grade for the enrollment as well as Crijns and colleagues did [12]. This is because a standard system for grading ovarian carcinomas is still under construction in the world, although several grading systems have been proposed for epithelial ovarian cancer [21–23,33,34]. According to the three criteria above, we recruited 110 Japanese ovarian cancer patients as a discovery set for the PFS analysis. The prognostic index for each patient was simply calculated by the ridge-regression-weighted sum of 88-gene expression values, and the prognostic power of our index was assessed using Tothill's dataset [20]. Further, subsequent stratified analysis according to debulking status, which was an independent prognostic factor in multivariate analysis of the discovery dataset, indicated that our prognostic index was associated with PFS time

Table 4. Univariate and multivariate Cox's proportional hazard model analysis of prognostic factors for overall survival.

	Univariate analysis		Multivariate analysis	
Prognostic factor	**Hazard ratio (95%CI*)**	***p*-value**	**Hazard ratio (95%CI)**	***p*-value**
A) Present study (n = 110)				
Age	1.01 (0.98–1.03)	0.56	-	-
Stage IV (vs Stage III)	1.14 (0.78–1.59)	0.49	0.75 (0.50–1.08)	0.12
Optimal Surgery (vs not optimal)	0.69 (0.50–0.92)	0.012	0.98 (0.70–1.35)	0.90
Grade				
Grade2 (vs Grade1)	1.30 (0.85–2.09)	0.23	1.23 (0.80–2.01)	0.35
Grade3 (vs Grade1)	1.68 (1.12–2.68)	0.012	1.83 (1.18–3.02)	0.0065
Prognostic Index				
High (vs Low)	2.72 (1.91–4.08)	<0.0001	2.99 (2.02–4.65)	<0.0001
B) Tothill's dataset [20] (n = 87)				
Age	1.01 (0.97–1.05)	0.73	1.00 (0.97–1.04)	0.88
Stage IV (vs Stage III)	2.13 (0.85–3.95)	0.093	1.60 (0.62–3.21)	0.28
Optimal Surgery (vs not optimal)	0.89 (0.62–1.23)	0.42	0.94 (0.66–1.37)	0.74
Prognostic Index				
High (vs Low)	1.76 (1.24–2.55)	0.0013	1.71 (1.20–2.49)	0.0029

*CI denotes confidence interval.

doi:10.1371/journal.pone.0009615.t004

independently of the debulking status. However, the sensitivity and specificity of the prognostic index for discriminating between early- and late-relapse patients were lower in Tothill's dataset than those in the discovery set. This might be caused by different backgrounds in respects of ethnicity or microarray platform. Although the differences in gene expression of cancer tissues among ethnicities have not been reported previously, several studies indicate that the proportions of clear cell and endometrioid histological types in

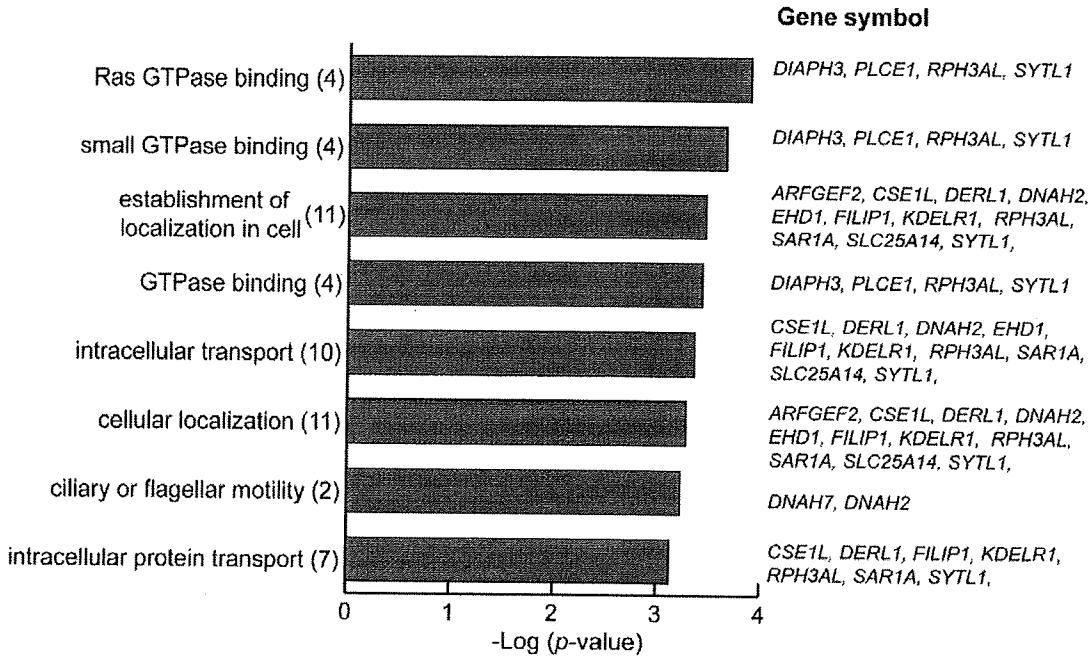

Figure 4. Biological characteristics of 88 progression-free survival-related genes. Significantly over-represented 8 gene ontology (GO) categories in GO-based profiling of 88 genes after multiple testing correction of the Benjamini–Hochberg false discovery rate method (FDR q-value≤0.10). Over-represented GO categories were identified using all genes on Agilent platform as a background set of genes for the determining p-values. The actual number of the PFS-related genes involved in each category is given in parentheses.

doi:10.1371/journal.pone.0009615.g004

epithelial ovarian cancer in Asian population are higher than those in non-Asian populations [35,36]. Recent genome-wide association study has identified a single nucleotide polymorphism at 9p22 associated with ovarian cancer risk in subjects with European ancestry but not in non-European descendants [37]. This type of differences between studies could be also attributed to genetic as well as environmental factors. In addition, we cannot rule out the possibility that the present PFS-associated classifiers with ridge-regression-based weights still have insufficient generalization properties on the external dataset due to the problem of overfitting. Therefore, we will reconsider these important issues such as between-study differences in ethnicities and microarray platforms and the overfitting problem using a larger number of microarray data from advanced-stage serous ovarian cancer patients in order to obtain better classifiers for the prediction of prognosis. And to improve the accuracy of prognostic index, development of prognostic index after the stratification of patients will be a research agenda for further study.

Interestingly, the present 88-gene prognostic index for prediction of PFS time was also significantly associated with overall survival time in both our dataset and Tothill's dataset [20]. Moreover, we examined the predictive ability of our prognostic index in Dressman's dataset [25] since patients in their dataset received longer-term follow-up than those in the above two datasets. Although Dressman's dataset (n = 119) [25] included 34 patients treated with platinum/cyclophospamide chemotherapy and 3 with single-agent platinum, the significance of this prognostic index for overall survival was still statistically supported in the longer followed-up dataset. As treatments for recurrent ovarian cancer patients remain an open area of investigation aiming to lead to survival benefit [38], our prognostic index for patient with advanced-stage serous ovarian cancer displays a potential to predict not only PFS time but also overall survival time. In the future, we may apply the prognostic indices to estimation of risk of recurrence for serous ovarian cancer patients and select a novel treatment such as dose-dense chemotherapy [39] or molecular-targeted agent for the purpose of improving prognosis of high-risk patients.

There are small number of genes overlapped between our 88 PFS-related profile and previously reported expression-profiles that were related to prognosis or sensitivity of platinum/taxane-based chemotherapy [11–15,40,41]. Konstantinopoulos *et al.* [6] have discussed that these discrepancies might be related to the use of different microarray platforms with different normalization methods and different degree of contamination by noncancerous cells in a tumor sample, as well as differences in the patient populations under study. Nevertheless, several survival-associated genes such as *E2F2* and *HLA-DMB* [42,43] are included in 88 PFS-related genes. Reimer *et al.* [42] have reported that *E2F2* is associated with grade 3 ovarian tumors and residual disease (more than 2cm in diameter) after initial surgery, and that low *E2F2* expression is significantly associated with favorable disease-free and overall survival in epithelial ovarian cancer. Callahan *et al.* [43] have recently reported that the high expression of HLA-DMB in ovarian cancer cells is correlated with increased numbers of tumor-infiltrating CD8-positive T lymphocytes, and with good prognosis in advanced-stage high-grade serous ovarian cancer.

We performed GO analysis and IPA to assess biological characteristics of PFS-related genes. GO analysis revealed the significant associations of GTPase binding, intracellular transport, and ciliary or flagellar motility with PFS (Figure 4). *PLCE1* belongs to the GTPase binding category and activates MAP kinase or ERK as shown in IPA network 3 (Figure S7). In particular, previous report indicates that *PLCE1* activates the small G protein Ras/MAP kinase signaling [44], which is one of important pathways associated with cell growth and differentiation. Intriguingly, *CSE1L* included in the intracellular transport category is involved in the regulation of multiple cellular mechanisms, proliferation, and apoptosis [45]. Tanaka *et al.* [46] have reported that *CSE1L* is associated with regulated expression of p53 target genes, and that downregulation of *CSE1L* protects cancer cell from DNA damage-induced apoptosis. *DNAH2* and *DNAH7* are components of the inner dynein arm of cilialy axonemes, and axonemal dyneins are molecular motors that drive the beating of cilia and flagella. Plotnikova *et al.* [47] have reported that loss of cilia in cancer cells may contribute to the insensitivity of cancer cells to environmental repressive signals, partly owing to derangement of cell cycle checkpoints governed by cilia and centrosomes. On the other hand, IPA analysis showed several genes interacting with *SRC* or *MYC* (Figure S6), each of which was reported as a representative gene in oncogenic pathways of ovarian cancer [25,27]. Dressman *et al.* [25] have demonstrated that Src pathway activity is associated with chemotherapy response because of a significant correlation between the activation of Src pathway and poor prognosis in patients with platinum-resistant ovarian cancer. *MYC* is a multifunctional proto-oncogene and activated in about 30% of ovarian cancer by several mechanisms [48]. Iba *et al.* [49] report that MYC expression is associated with responsiveness to platinum-based chemotherapy and with prognosis in patients with epithelial ovarian cancer. Our PFS-related profile might have potentially functional relevance to altered activities of several oncogenic pathways. Although we identified several genes whose molecular function could be linked to prognosis in ovarian cancer patients, further functional study will be necessary to clarify the biological and pathological implications of the PFS-related profile.

These results suggest that the gene expression profile could be a useful tool to predict disease progression or recurrence of advanced-stage serous ovarian cancer. To apply the gene expression profile in clinical practice, we will need to improve the predictive ability of the profile and confirm the reliability of survival profile in a prospective multi-center study. Nevertheless, the survival-related profile could provide an optimization of the clinical management and development of new therapeutic strategies for the serous ovarian cancer patients.

Materials and Methods

Tissue Samples

One hundred ten Japanese patients who were diagnosed with advanced-stage serous ovarian cancer between July 1997 and June 2008 were included in this study. Fresh-frozen samples were obtained from primary tumor tissues during primary debulking surgery prior to chemotherapy. All patients with advanced-stage serous ovarian cancer were treated with platinum/taxane-based chemotherapy after surgery. In principle, patients were seen every 1 to 3 months for the first 2 years. Thereafter, follow-up visits had an interval of 3 to 6 months in the third to fifth year, and 6 to 12 months in the sixth to tenth year. At every follow-up visits, general physical and gynecologic examination were performed. CA125 serum levels were routinely determined. Staging of the disease was assessed according to the criteria of the International Federation of Gynecology and Obstetrics (FIGO) [19]. Optimal debulking surgery was defined as ≤1cm of gross residual disease. The histological characteristics of surgically resected specimens were assessed on formalin-fixed and paraffin-embedded hematoxylin and eosin sections by two or three gynecological pathologists belonging to the Japanese Society of Pathology at each institute,

and frozen tissues containing more than 80% of tumor cells upon histological evaluation were used for RNA extraction. In this study, the degree of histological differentiation is determined according to the increase in the proportion of solid growth within the adenocarcinoma as follows: grade 1, less than 5% solid growth; grade 2, 6-50% solid growth; grade 3, over 50% solid growth based on grading system proposed by Japan Society of Gynecologic Oncology.

PFS time was calculated as the interval from primary surgery to disease progression or recurrence. Based on standard Response Evaluation Criteria In Solid Tumors (RECIST) guidelines [50], disease progression was defined as at least 20% increase in the sum of the longest diameters of all target lesions or as the appearance of one or more new lesions and/or unequivocal progression existing non-target lesions. Overall survival time was calculated as the interval from primary surgery to the death due to ovarian cancer. This study was approved by the institutional ethics review board at Niigata University (No. 239, 282, 285, and 318), Niigata Cancer Center Hospital (No. 25), Jichi Medical University (G07-01), Kagoshima City Hospital (H19-21), Hiroshima University (Hi-11), Nagasaki University (080509), Kumamoto University (No. 309), and Tokai University (07I-29). All patients provided written informed consent for the collection of samples and subsequent analysis.

Microarray Experiments

Total RNA was extracted from tissue samples as previously described [17]. Five hundred nanograms of total RNA were converted into labeled cRNA with nucleotides coupled to a cyanine 3-CTP (Cy3) (PerkinElmer, Boston, MA, USA) using the Quick Amp Labeling Kit, one-color (Agilent Technologies). Cy3-labeled cRNA (1.65 μg) was hybridized for 17 hours at 65°C to an Agilent Whole Human Genome Oligo Microarray, which carries 60-mer probes to more than 40,000 human transcripts. The hybridized microarray was washed and then scanned in Cy3 channel with the Agilent DNA Microarray Scanner (model G2565AA). Signal intensity per spot was generated from the scanned image using Feature Extraction Software version 9.1 (Agilent Technologies) in the default settings. Spots that did not pass quality control procedures were flagged as "Absent". The MIAME-compliant microarray data were deposited into the Gene Expression Omnibus data repository (accession number GSE17260).

Microarray Data Analysis

We analyzed our dataset as a "discovery set" and the publicly available dataset as an "external dataset". Considering differences in microarray platforms, we selected common genes between the Agilent Whole Human Genome Oligo Microarray and Affymetrix Human Genome U133 Plus 2.0 Array, which was the platform in an external dataset (GSE9891) [20].

Data normalization was performed in GeneSpring GX 10 (Agilent Technologies) as follows: (i) Threshold raw signals were set to 1.0, (ii) 75th percentile normalization was chosen as normalized algorithm, (iii) Baseline was transformed to median of all samples. Furthermore, the expression level was normalized by Z-transformation (the mean expression was set to 0 and standard deviation to 1 for each gene in each dataset). In our dataset, 18,178 probes with expression levels marked as "Present" in all microarrays were used to remove missing and uncertain signals on gene expression.

The PFS-related genes from the 18,178 probes were identified by univariate Cox proportional hazard analysis, followed by a ridge regression, a penalized Cox regression analysis for survival prediction (Figure S2). We first identified 97 probes with expression levels correlating with the PFS time determined using the univariate Cox proportional hazard model ($p<0.01$). In case of multiple probes representing a given gene (so-called multiple tagged gene) in microarrays, only the probe with the largest magnitude (i.e., sum of the squares of per-individual expression values) was extracted as a representative probe for the gene [24]. To avoid the problem of overfitting, ridge regression extension of the multivariate Cox model was employed [18]. The ridge regression shrinks regression coefficients (β) of genes in multivariate Cox model by imposing a penalty on squared values of the coefficients, and is able to handle the problem of having larger number of expression values than individuals in an appropriate way [30]. We estimated regression coefficients of the prognostic genes by the ridge regression Cox model using M-files (available at http://www.med.uio.no/imb/stat/bmms/software/microsurv/) for MATLAB (Mathworks, Natick, MA, USA). Using 10-fold cross-validation, we obtained regression coefficients with optimal penalty parameter for the penalized Cox model, and calculated a prognostic index for each patient as defined by

$$\text{Prognostic index} = \sum_{i=1}^{88} \beta_i \times X_i \qquad (1)$$

where β_i is the estimated regression coefficient of each gene in discovery dataset under ridge regression multivariate Cox model and X_i is the Z-transformed expression value of each gene [18]. The estimated regression coefficient of each PFS-related gene given by ridge regression in the discovery set was also applied to calculate a prognostic index for each patient in external dataset using the equation above. We classified all patients into the two groups (high- and low-risk groups) by the median of the prognostic index in discovery set [9]. PFS between high- and low-risk groups was compared using Kaplan-Meier curves and the log rank test using GraphPad PRISM version 4.0 (GraphPad Software, San Diego, CA, USA). Furthermore, We then evaluated the prognostic index in the multivariate Cox proportional hazard model using JMP version 6 (SAS Institute, Cary, NC, USA). We also examined the discrimination performance of the prognostic index between early and late relapse in patients by plotting a receiver operating characteristic (ROC) curve for each dataset (JMP). Because 18 months is the median PFS time for advanced-stage ovarian cancer patients treated with cisplatin-paclitaxel [1], we used 18 months as the cut-off between early and late relapse. We performed ROC curve analysis for our prognostic index in only patients with follow-up for more than 18 months (Discovery set 103 samples; External dataset 84 samples).

To investigate the biological functions of PFS-related gene expression profiles, we used GO Ontology Browser, embedded in GeneSpring GX [17,51]. The GO Ontology Browser was used to analyze which categories of gene ontology were statistically overrepresented among the gene list obtained. Statistical significance was determined by Fisher's exact test, followed by multiple testing corrections by the Benjamini and Hochberg false discovery rate (FDR) method [26]. Furthermore, we tried to explore molecular interaction networks among the PFS-related genes using Ingenuity Pathway Analysis (IPA) [17].

Quantitative Real-Time Reverse Transcription Polymerase Chain Reaction (RT-PCR) Analysis

Real-time PCR was performed on *E2F2* (Hs00231667_m1, Applied Biosystems), *FOXJ1* (Hs00230964_m1, Applied Biosystems), *DNAH7* (Hs01022427_m1, Applied Biosystems), and *FILIP1* (Hs00325074_m1, Applied Biosystems) for a subset of serous

ovarian cancer (n = 53) as previously described [17]. The relative quantification method [52] was used to measure the amounts of the respective genes in serous ovarian cancer samples, normalized to *ACTB* (Hs99999903_m1, Applied Biosystems) and *TBP* (Hs99999910_m1, Applied Biosystems).

Evaluation of PFS-Related Genes in the External Dataset

To confirm whether our expression profile could predict prognosis of serous ovarian cancer patients in an independent data set, we selected to use publicly available microarray data (GSE9891) only because the data also disclosed individual clinical characteristics including PFS time. We examined clinical information of these dataset using supplementary data [20]. From this original dataset (n = 285), we selected 87 samples that were (i) diagnosed as advanced-stage serous adenocarcinoma, (ii) treated by platinum/taxane-based chemotherapy, (iii) obtained from primary lesion, and (iv) followed-up for more than 12 months (Table S1). Their samples are histologically graded by Silverberg classification [22] whose grading system is different from that in this study.

Supporting Information

Figure S1 Kaplan-Meier survival curves between 110 patients in this dataset and 87 in Tothill's dataset.
Found at: doi:10.1371/journal.pone.0009615.s001 (0.24 MB TIF)

Figure S2 Analytical process to develop a prognostic index for predicting survival.
Found at: doi:10.1371/journal.pone.0009615.s002 (0.48 MB TIF)

Figure S3 Assessment of the sensitivity and specificity of 88-gene prognostic index using receiver-operating characteristic (ROC) curves. When early relapse is positive in the analysis, the area under ROC curve to distinguish early-relapse patients with less than 18 months of progression-free survival times from late-relapse patients was 0.959 and 0.674 in (A) discovery set (early, n = 54; late, n = 49) and in (B) external set (early, n = 45; late, n = 39), respectively.
Found at: doi:10.1371/journal.pone.0009615.s003 (0.42 MB TIF)

Figure S4 Appling PFS-related gene expression profile to Dressman's dataset [25]. (A) Multivariate analysis showed a significant association of overall survival with the prognostic index estimated using the 88-gene linear combination model with the ridge regression coefficients from the present discovery set in Dresssman's dataset (HR, 1.51; 95% CI, 1.19–1.93, p = 0.0008) (B) Kaplan-Meier survival curves and the log rank test showed that high-risk patients had shorter overall survival compared to low-risk patients (median survival, 31 and 87 months for high- and low-risk patients, respectively; p = 0.0008).
Found at: doi:10.1371/journal.pone.0009615.s004 (0.23 MB TIF)

Figure S5 Molecular interaction networks of 88 progression-free survival-related genes using Ingenuity Pathway Analysis (IPA) software. The prognostic genes incorporated into the respective networks were marked as gray-colored.
Found at: doi:10.1371/journal.pone.0009615.s005 (2.42 MB TIF)

Figure S6 Molecular interaction networks of 88 progression-free survival-related genes using Ingenuity Pathway Analysis (IPA) software. The prognostic genes incorporated into the respective networks were marked as gray-colored.
Found at: doi:10.1371/journal.pone.0009615.s006 (1.68 MB TIF)

Figure S7 Molecular interaction networks of 88 progression-free survival-related genes using Ingenuity Pathway Analysis (IPA) software. The prognostic genes incorporated into the respective networks were marked as gray-colored.
Found at: doi:10.1371/journal.pone.0009615.s007 (1.82 MB TIF)

Table S1 Clinical characteristics of advanced-stage serous ovarian cancer patients in Tothill's dataset [20] (n = 87).
Found at: doi:10.1371/journal.pone.0009615.s008 (0.04 MB DOC)

Table S2 Univariate and multivariate Cox's proportional hazard model analysis of prognostic factors for progression-free survival.
Found at: doi:10.1371/journal.pone.0009615.s009 (0.04 MB DOC)

Table S3 Univariate Cox's proportional hazard model analysis of prognostic index for progression-free survival in the two datasets.
Found at: doi:10.1371/journal.pone.0009615.s010 (0.04 MB DOC)

Acknowledgments

We thank tissue donors and supporting medical staff for making this study possible. We are grateful to C. Seki and A. Yukawa for their technical assistance.

Author Contributions

Conceived and designed the experiments: KY AT TY H KT. Performed the experiments: KY AT. Analyzed the data: KY AT. Contributed reagents/materials/analysis tools: KY TY SK HF MS YO MH KS HF YK KK HM HT HK H KT. Wrote the paper: KY AT TY H KT.

References

1. McGuire WP, Hoskins WJ, Brady MF, Kucera PR, Partridge EE, et al. (1996) Cyclophosphamide and cisplatin compared with paclitaxel and cisplatin in patients with stage III and stage IV ovarian cancer. N Engl J Med 334: 1–6.
2. Piccart MJ, Bertelsen K, James K, Cassidy J, Mangioni C, et al. (2000) Randomized intergroup trial of cisplatin-paclitaxel versus cisplatin-cyclophosphamide in women with advanced epithelial ovarian cancer: three-year results. J Natl Cancer Inst 92: 699–708.
3. Cannistra SA (2004) Cancer of the ovary. N Engl J Med 351: 2519–29.
4. du Bois A, Reuss A, Pujade-Lauraine E, Harter P, Ray-Coquard I, et al. (2009) Role of surgical outcome as prognostic factor in advanced epithelial ovarian cancer: a combined exploratory analysis of 3 prospectively randomized phase 3 multicenter trials: by the Arbeitsgemeinschaft Gynaekologische Onkologie Studiengruppe Ovarialkarzinom (AGO-OVAR) and the Groupe d'Investigateurs Nationaux Pour les Etudes des Cancers de l'Ovaire (GINECO). Cancer 115: 1234–44.
5. Winter WE, 3rd, Maxwell GL, Tian C, Carlson JW, Ozols RF, et al. (2007) Prognostic factors for stage III epithelial ovarian cancer: a Gynecologic Oncology Group Study. J Clin Oncol 25: 3621–7.
6. Konstantinopoulos PA, Spentzos D, Cannistra SA (2008) Gene-expression profiling in epithelial ovarian cancer. Nat Clin Pract Oncol 5: 577–87.
7. van 't Veer LJ, Dai H, van de Vijver MJ, He YD, Hart AA, et al. (2002) Gene expression profiling predicts clinical outcome of breast cancer. Nature 415: 530–6.
8. Motoori M, Takemasa I, Yano M, Saito S, Miyata H, et al. (2005) Prediction of recurrence in advanced gastric cancer patients after curative resection by gene expression profiling. Int J Cancer 114: 963–8.
9. Chen HY, Yu SL, Chen CH, Chang GC, Chen CY, et al. (2007) A five-gene signature and clinical outcome in non-small-cell lung cancer. N Engl J Med 356: 11–20.
10. Schramm A, Schulte JH, Klein-Hitpass L, Havers W, Sieverts H, et al. (2005) Prediction of clinical outcome and biological characterization of neuroblastoma by expression profiling. Oncogene 24: 7902–12.
11. Bonome T, Levine DA, Shih J, Randonovich M, Pise-Masison CA, et al. (2008) A gene signature predicting for survival in suboptimally debulked patients with ovarian cancer. Cancer Res 68: 5478–86.
12. Crijns AP, Fehrmann RS, de Jong S, Gerbens F, Meersma GJ, et al. (2009) Survival-related profile, pathways, and transcription factors in ovarian cancer. PLoS Med 6: e24.
13. Denkert C, Budczies J, Darb-Esfahani S, Györffy B, Sehouli J, et al. (2009) A prognostic gene expression index in ovarian cancer - validation across different independent data sets. J Pathol 218: 273–80.

14. Hartmann LC, Lu KH, Linette GP, Cliby WA, Kalli KR, et al. (2005) Gene expression profiles predict early relapse in ovarian cancer after platinum-paclitaxel chemotherapy. Clin Cancer Res 11: 2149–55.
15. Spentzos D, Levine DA, Ramoni MF, Joseph M, Gu X, et al. (2004) Gene expression signature with independent prognostic significance in epithelial ovarian cancer. J Clin Oncol 22: 4700–10.
16. Agarwal R, Kaye SB (2006) Expression profiling and individualization of treatment for ovarian cancer. Curr Opin Pharmacol 6: 345–9.
17. Yoshihara K, Tajima A, Komata D, Yamamoto T, Kodama S, et al. (2009) Gene expression profiling of advanced-stage serous ovarian cancers distinguishes novel subclasses and implicates ZEB2 in tumor progression and prognosis. Cancer Sci 100: 1421–8.
18. Bøvelstad HM, Nygård S, Størvold HL, Aldrin M, Borgan O, et al. (2007) Predicting survival from microarray data–a comparative study. Bioinformatics 23: 2080–7.
19. FIGO Cancer Committee. (1986) Staging Announcement: FIGO Cancer Committee. Gynecol Oncol 25: 383–5.
20. Tothill RW, Tinker AV, George J, Brown R, Fox SB, et al. (2008) Novel molecular subtypes of serous and endometrioid ovarian cancer linked to clinical outcome. Clin Cancer Res 14: 5198–208.
21. International Federation of Gynecology and Obstetrics (1971) Classification and staging of malignant tumours in the female pelvis. Acta Obstet Gynecol Scand 50: 1–7.
22. Silverberg SG (2000) Histopathologic grading of ovarian carcinoma: a review and proposal. Int J Gynecol Pathol 19: 7–15.
23. Kommoss S, Schmidt D, Kommoss F, Hedderich J, Harter P, et al. (2009) Histological grading in a large series of advanced stage ovarian carcinomas by three widely used grading systems: consistent lack of prognostic significance. A translational research subprotocol of a prospective randomized phase III study (AGO-OVAR 3 protocol). Virchows Arch 454: 249–56.
24. Woo HG, Park ES, Cheon JH, Kim JH, Lee JS, et al. (2008) Gene expression-based recurrence prediction of hepatitis B virus-related human hepatocellular carcinoma. Clin Cancer Res 14: 2056–64.
25. Dressman HK, Berchuck A, Chan G, Zhai J, Bild A, et al. (2007) An integrated genomic-based approach to individualized treatment of patients with advanced-stage ovarian cancer. J Clin Oncol 25: 517–25.
26. Benjamini Y, Hochberg Y (1995) Controlling the false discovery rate: a practical and powerful approach to multiple testing. J R Statist Soc B 57: 289–300.
27. Bild AH, Yao G, Chang JT, Wang Q, Potti A, et al. (2006) Oncogenic pathway signatures in human cancers as a guide to targeted therapies. Nature 439: 353–7.
28. Dupuy A, Simon RM (2007) Critical review of published microarray studies for cancer outcome and guidelines on statistical analysis and reporting. J Natl Cancer Inst 99: 147–57.
29. Bair E, Tibshirani R (2004) Semi-supervised methods to predict patient survival from gene expression data. PLoS Biol 2: e108.
30. van Houwelingen HC, Bruinsma T, Hart AA, Van't Veer LJ, Wessels LF (2006) Cross-validated Cox regression on microarray gene expression data. Stat Med 25: 3201–16.
31. Rosenwald A, Wright G, Chan WC, Connors JM, Campo E, et al. (2002) The use of molecular profiling to predict survival after chemotherapy for diffuse large-B-cell lymphoma. N Engl J Med 346: 1937–47.
32. Sorlie T, Tibshirani R, Parker J, Hastie T, Marron JS, et al. (2003) Repeated observation of breast tumor subtypes in independent gene expression data sets. Proc Natl Acad Sci U S A 100: 8418–23.
33. Tawassoli FA, Devilee P (2003) Pathology and Genetics. Tumours of the Breast and Female Genital Organs. IARC Press, Lyon.
34. Malpica A, Deavers MT, Lu K, Bodurka DC, Atkinson EN, et al. (2004) Grading ovarian serous carcinoma using a two-tier system. Am J Surg Pathol 28: 496–504.
35. Goodman MT, Howe HL, Tung KH, Hotes J, Miller BA, et al. (2003) Incidence of ovarian cancer by race and ethnicity in the United States, 1992–1997. Cancer 97(10 Suppl): 2676–85.
36. McGuire V, Jesser CA, Whittemore AS (2002) Survival among U.S. women with invasive epithelial ovarian cancer. Gynecol Oncol 84: 399–403.
37. Song H, Ramus SJ, Tyrer J, Bolton KL, Gentry-Maharaj A, et al. (2009) A genome-wide association study identifies a new ovarian cancer susceptibility locus on 9p22.2. Nat Genet 41: 996–1000.
38. Ozols RF (2005) Treatment goals in ovarian cancer. Int J Gynecol Cancer 15 Suppl 1: 3–11.
39. Katsumata N, Yasuda M, Takahashi F, Isonishi S, Jobo T, et al. (2009) Dose-dense paclitaxel once a week in combination with carboplatin every 3 weeks for advanced ovarian cancer: a phase 3, open-label, randomised controlled trial. Lancet 374: 1331–8.
40. Berchuck A, Iversen ES, Luo J, Clarke JP, Horne H, et al. (2009) Microarray analysis of early stage serous ovarian cancers shows profiles predictive of favorable outcome. Clin Cancer Res 15: 2448–55.
41. Helleman J, Jansen MP, Span PN, van Staveren IL, Massuger LF, et al. (2006) Molecular profiling of platinum resistant ovarian cancer. Int J Cancer 118: 1963–71.
42. Reimer D, Sadr S, Wiedemair A, Stadlmann S, Concin N, et al. (2007) Clinical relevance of E2F family members in ovarian cancer–an evaluation in a training set of 77 patients. Clin Cancer Res 13: 144–51.
43. Callahan MJ, Nagymanyoki Z, Bonome T, Johnson ME, Litkouhi B, et al. (2008) Increased HLA-DMB expression in the tumor epithelium is associated with increased CTL infiltration and improved prognosis in advanced-stage serous ovarian cancer. Clin Cancer Res 14: 7667–73.
44. Lopez I, Mak EC, Ding J, Hamm HE, Lomasney JW (2001) A novel bifunctional phospholipase c that is regulated by Galpha 12 and stimulates the Ras/mitogen-activated protein kinase pathway. J Biol Chem 276: 2758–65.
45. Behrens P, Brinkmann U, Wellmann A (2003) CSE1L/CAS: its role in proliferation and apoptosis. Apoptosis 8: 39–44.
46. Tanaka T, Ohkubo S, Tatsuno I, Prives C (2007) hCAS/CSE1L associates with chromatin and regulates expression of select p53 target genes. Cell 130: 638–50.
47. Plotnikova OV, Golemis EA, Pugacheva EN (2008) Cell cycle-dependent ciliogenesis and cancer. Cancer Res 68: 2058–61.
48. Darcy KM, Brady WE, Blancato JK, Dickson RB, Hoskins WJ, et al. (2009) Prognostic relevance of c-MYC gene amplification and polysomy for chromosome 8 in suboptimally-resected, advanced stage epithelial ovarian cancers: a Gynecologic Oncology Group study. Gynecol Oncol 114: 472–9.
49. Iba T, Kigawa J, Kanamori Y, Itamochi H, Oishi T, et al. (2004) Expression of the c-myc gene as a predictor of chemotherapy response and a prognostic factor in patients with ovarian cancer. Cancer Sci 95: 418–23.
50. Therasse P, Arbuck SG, Eisenhauer EA, Wanders J, Kaplan RS, et al. (2000) New guidelines to evaluate the response to treatment in solid tumors. European Organization for Research and Treatment of Cancer, National Cancer Institute of the United States, National Cancer Institute of Canada. J Natl Cancer Inst 92: 205–16.
51. Okada H, Tajima A, Shichiri K, Tanaka A, Tanaka K, et al. (2008) Genome-wide expression of azoospermia testes demonstrates a specific profile and implicates ART3 in genetic susceptibility. PLoS Genet 4: e26.
52. Livak KJ, Schmittgen TD (2001) Analysis of Relative Gene Expression Data Using Real-Time Quantitative PCR and the $2^{-\Delta\Delta CT}$ Method. Methods 25: 402–8.

nature
cell biology

The lipid droplet is an important organelle for hepatitis C virus production

Yusuke Miyanari[1,2], Kimie Atsuzawa[3], Nobuteru Usuda[3], Koichi Watashi[1,2], Takayuki Hishiki[1,2], Margarita Zayas[4], Ralf Bartenschlager[4], Takaji Wakita[5], Makoto Hijikata[1,2] and Kunitada Shimotohno[1,2,6]

The lipid droplet (LD) is an organelle that is used for the storage of neutral lipids. It dynamically moves through the cytoplasm, interacting with other organelles, including the endoplasmic reticulum (ER)[1–3]. These interactions are thought to facilitate the transport of lipids and proteins to other organelles. The hepatitis C virus (HCV) is a causative agent of chronic liver diseases[4]. HCV capsid protein (Core) associates with the LD[5], envelope proteins E1 and E2 reside in the ER lumen[6], and the viral replicase is assumed to localize on ER-derived membranes. How and where HCV particles are assembled, however, is poorly understood. Here, we show that the LD is involved in the production of infectious virus particles. We demonstrate that Core recruits nonstructural (NS) proteins and replication complexes to LD-associated membranes, and that this recruitment is critical for producing infectious viruses. Furthermore, virus particles were observed in close proximity to LDs, indicating that some steps of virus assembly take place around LDs. This study reveals a novel function of LDs in the assembly of infectious HCV and provides a new perspective on how viruses usurp cellular functions.

Hepatitis C virus (HCV) has a plus-strand RNA genome that encodes the viral structural proteins Core, E1 and E2, the p7, and the nonstructural (NS) proteins 2, 3, 4A, 4B, 5A and 5B (refs 7, 8). NS proteins are reported to localize on the cytoplasmic side of endoplasmic reticulum (ER) membranes[9]. To elucidate the mechanisms of virus production, we used a HCV strain, JFH1, which can produce infectious viruses[10–12]. We first investigated the subcellular localization of the HCV proteins in cells that had been transfected with JFH1^{E2FL} RNA, in which a part of the hypervariable region 1 of E2 was replaced by the FLAG epitope tag (see Supplementary Information, Fig. S1, S2a–d). Core localized to the lipid droplets (LDs; Fig. 1a), as previously reported[5]. Interestingly, NS proteins were also detected around LDs in 60–90% of JFH1^{E2FL}-replicating cells (Fig. 1a, c). Similar levels of colocalization of LDs with viral proteins were observed in cells that had been transfected with chimeric HCV genomes expressing structural proteins, p7 and part of NS2 of the genotype 1b (Con1) or the genotype 1a (H77) isolate (see Supplementary Information, Fig. S1, S2e)[13]. In contrast, there was no close association between the LDs and NS proteins in cells that had been transfected with JFH1^{dC3} RNA (Fig. 1b, c), which lacked the coding region of Core (Supplementary Information, Fig. S1). NS proteins were diffusely present on the ER, suggesting that NS proteins are translocated from the ER to LDs in JFH1^{E2FL}-replicating cells in a Core-dependent manner. Importantly, there was no association between LDs and PDI, an ER marker protein, indicating that either ER membranes were absent in close proximity to LDs or that PDI was excluded from such membranes (Fig. 1c). These results were supported by western blot analysis of the LD fraction (Fig. 1d). The LD fraction contained ADRP, an LD marker, but not the ER markers Calnexin and Grp78 (data not shown), indicating that there was no ER contamination in the LD fraction. However, the LD fraction from JFH1^{E2FL}-replicating cells contained high levels of viral proteins in contrast to the LD fraction from JFH1^{dC3}-replicating cells (in which HCV proteins were virtually absent (Fig. 1d, LD fraction)), even though the expression levels of the NS proteins in whole-cell extracts were similar (Fig. 1d, whole-cell extract). About 20–45% of the total HCV proteins associated with the LDs in JFH1^{E2FL}-replicating cells (Fig. 1e). Consistent with previous reports that Core enhances the formation of LDs[14], overproduction of LDs was observed in JFH1^{E2FL}-, but not JFH1^{dC3}-replicating cells (Supplementary Information, Fig. S3a–l). Treatment of the cells with oleic acid, which enhanced the formation of LDs, did not affect either HCV protein levels or the recruitment of viral proteins to LDs in JFH1^{dC3}-replicating cells (Supplementary Information, Fig. S3m–p). Thus, the overproduction of LDs is insufficient for the recruitment of HCV proteins to LDs. To examine the ability of Core to recruit NS proteins to LDs, JFH1^{dC3}-replicating cells were transfected with a plasmid-expressing Core (Core^{WT}) (Fig. 1f, g). NS5A accumulated around LDs (Fig. 1f, arrowheads and panel 2), as did NS3 and NS4AB (Fig. 1g), in cells expressing Core^{WT}. The translocation of NS proteins to LDs was, however, not observed in JFH1^{dC3}-replicating cells expressing Core$^{PP/AA}$ (Fig. 1g and Supplementary Information, Fig. S2f–h),

[1]Department of Viral Oncology, Institute for Virus Research, Kyoto University, Kyoto 606-8507, Japan; [2]Graduate School of Biostudies, Kyoto University, Kyoto 606-8507, Japan; [3]Department of Anatomy, Fujita Health University School of Medicine, Toyoake 470-1192, Japan; [4]Department of Molecular Virology, University of Heidelberg, 69120 Heidelberg, Germany; [5]Department of Virology II, National Institute of Infectious Diseases, Tokyo 162-8640, Japan
[6]Correspondence should be addressed to K.S. (e-mail: shimkuni@z8.keio.jp)

Received 16 March 2007; accepted 31 July 2007; published online 26 August 2007; DOI: 10.1038/ncb1631

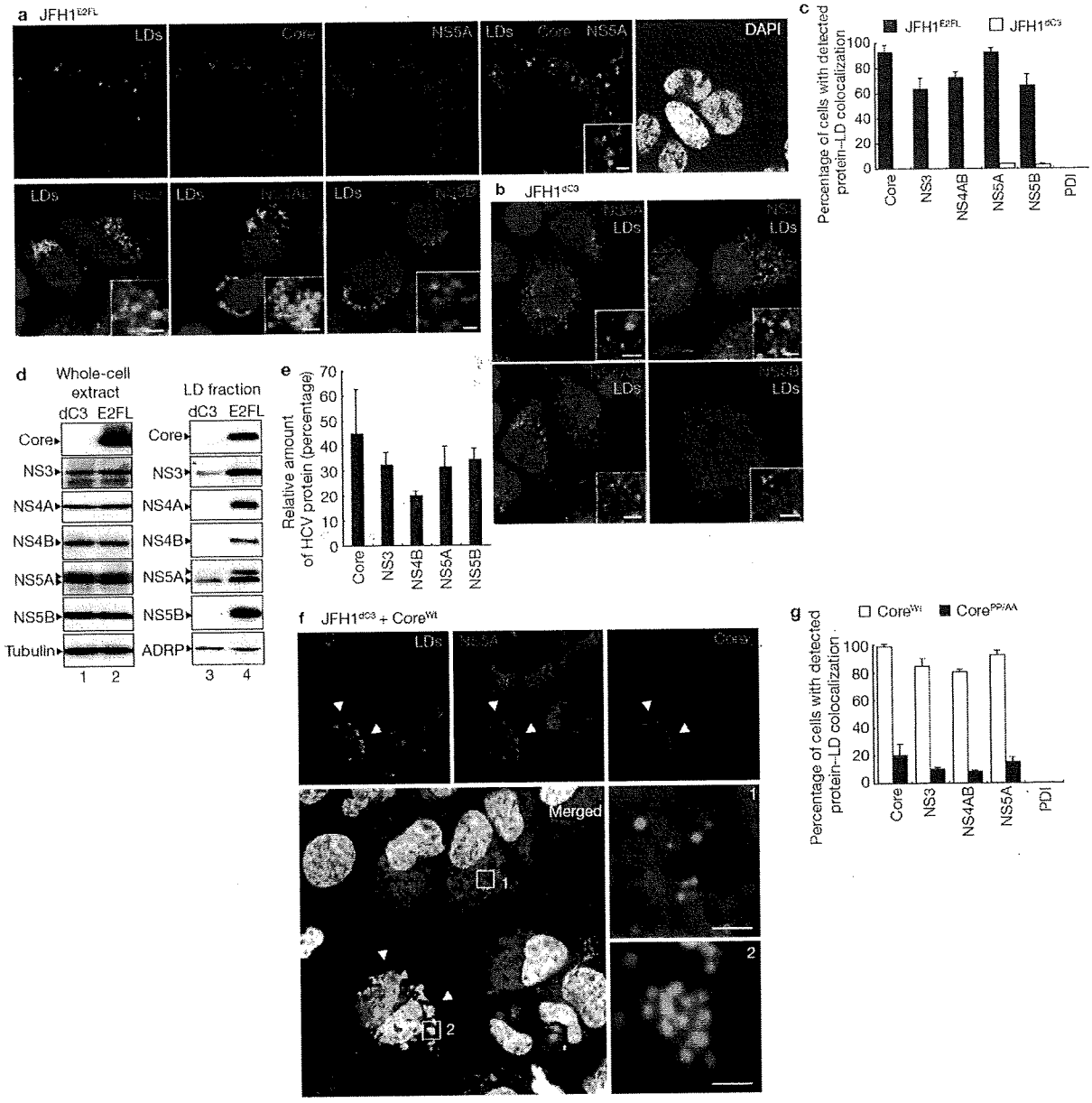

Figure 1 Core recruits NS proteins to LDs. (**a**) Huh-7 cells transfected with JFH1^{E2FL} RNA were labelled with antibodies against Core (red), NS5A (blue), NS3 (red), NS4AB (red) or NS5B (red). Lipid droplets (LDs) and nuclei were stained with BODYPI 493/503 (green) and DAPI (white in upper panel, blue in lower panels), respectively. Insets are high magnification images of areas in the respective panel. (**b**) JFH1^{dC3} replicon-bearing cells were labelled with DAPI (blue), BODIPY 493/503 (green) and indicated antibodies (red). The insets are high magnifications of the corresponding panel. (**c**) Percentages of JFH1^{E2FL}- or JFH1^{dC3}-bearing cells in which hepatitis C virus (HCV) proteins or PDI colocalize with LDs ($n > 200$). (**d**) Western blot analysis of HCV proteins and marker proteins in whole-cell extracts and the LD fractions from cells transfected with JFH1^{E2FL} (E2FL) or JFH1^{dC3} (dC3) RNA. (**e**) HCV proteins were quantified by using western blotting data of the purified LD fraction and whole-cell extracts of JFH1^{E2FL}-replicating cells. Results are shown as relative amounts of HCV proteins co-fractionated with LDs. This results correspond well with results obtained by quantitative immunofluorescence staining (data not shown). (**f**) Trans-complementation with Core^{Wt} relocates NS proteins to LDs. JFH1^{dC3} replicon-bearing cells were transfected with pcDNA3–Core^{Wt} and labelled with BODIPY 493/503 (green), DAPI (white) and antibodies against NS5A (red) and Core (blue). Arrowheads indicate Core^{Wt}-expressing cells. Higher-magnification images of area 1 and area 2 are shown in panels 1 and 2, respectively. Scale bars, 2 μm. (**g**) The percentages of cells in which HCV proteins colocalize with LDs in the presence of Core^{Wt} or Core $^{PP/AA}$ ($n > 200$). Uncropped images of gels are shown in Supplementary Information Fig. S6. All error bars are derived from s.d.

a variant of Core containing two alanine substitutions at amino-acid positions 138 and 143 that fails to associate with LDs[15]. These results show that LD-associated Core recruits NS proteins from the ER to LDs.

Next, we investigated whether Core also recruited HCV RNA to LDs. *In situ* hybridization analysis showed that in more than 80% of JFH1^{E2FL}-replicating cells, both plus- and minus-strand RNAs were diffusely

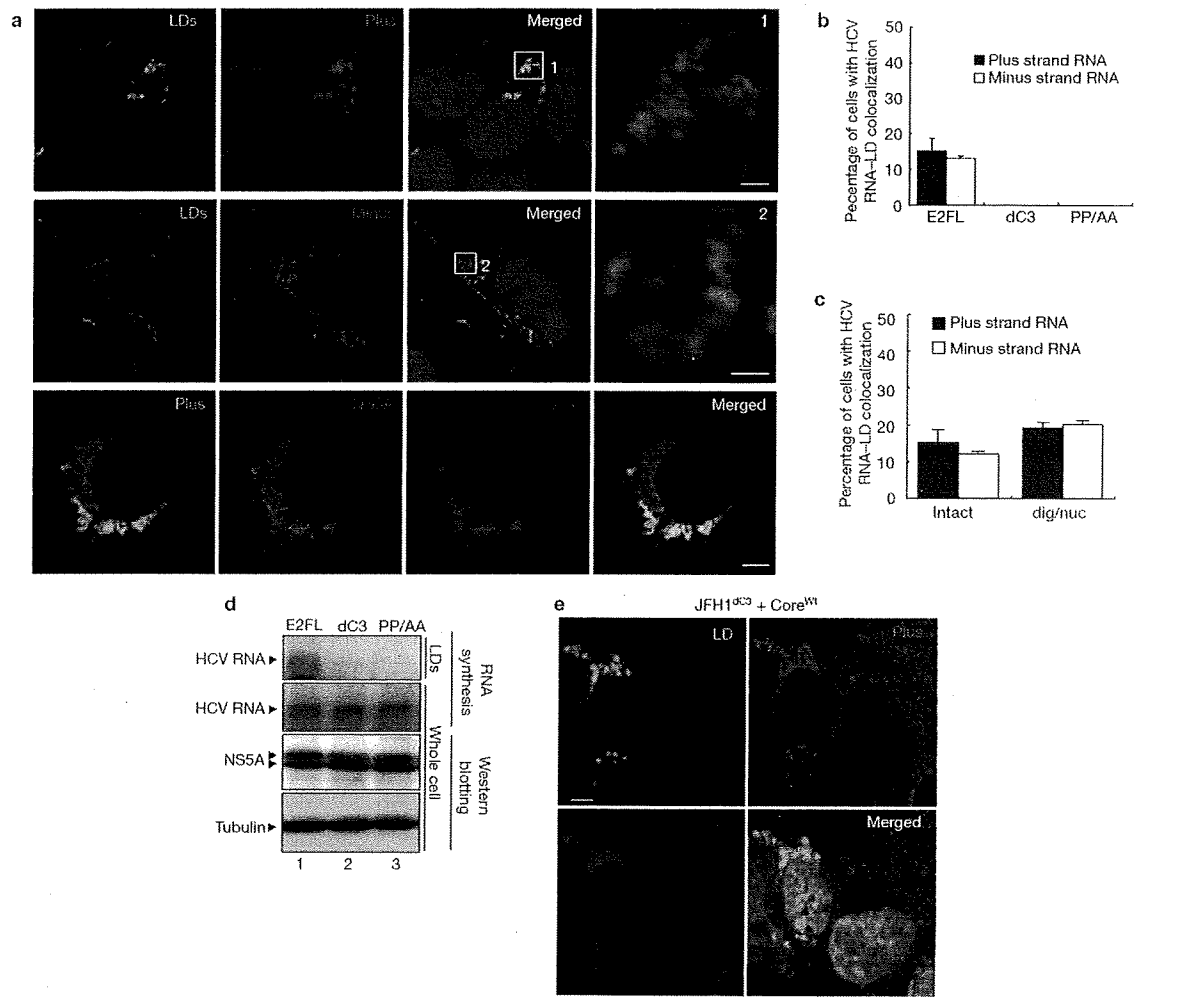

Figure 2 Core-dependent recruitment of active HCV replication complexes to the LD. (**a**) Huh-7 cells transfected with JFH1^{E2FL} RNA were analysed by *in situ* hybridization with strand-specific probes (plus or minus). The cells were labelled to simultaneously visualize lipid droplets (LDs), NS5A and Core (lower panels). Higher-magnification images of area 1 and area 2 are shown in the upper and middle right panels 1 and 2, respectively. Scale bars: 2 μm (panels 1, 2); 10 μm (lower right panel). (**b**) The percentages of JFH1^{E2FL}-, JFH1^{dC3}- and JFH1$^{PP/AA}$-expressing cells positive for overlapping signals for LDs and plus- or minus-strand hepatitis C virus (HCV) RNA ($n > 200$). (**c**) Intact or digitonin and nuclease-treated (dig/nuc) JFH1^{E2FL} replicon-bearing cells were analysed by *in situ* hybridization. The percentages of cells with overlapping signals for LD and plus- or minus-strand HCV RNA are shown ($n > 200$). (**d**) RNA-synthesizing activity in the LD fractions purified from cells transfected with JFH1^{E2FL}, JFH1^{dC3} or JFH1$^{PP/AA}$ RNA (top panel). As a control, HCV RNA synthesis activity in digitonin-permeabilized cells was analysed (second panel from the top). HCV protein levels represented by NS5A are shown, together with the level of tubulin (bottom two panels). (**e**) Localization of plus-strand HCV RNA and Core in JFH1^{dC3} replicon-bearing cells transfected with pcDNA3–Core^{Wt} (Scale bar, 10 μm). Uncropped images of gels are shown in Supplementary Information Fig. S6. All error bars are derived from s.d.

located in the perinuclear region (see Supplementary Information, Fig. S4a). More importantly, in about 20% of these cells, plus- and minus-strand RNAs accumulated around LDs (Fig. 2a, upper and middle panels; 2b) and colocalized with HCV proteins such as Core and NS5A (Fig. 2a, lower panels). No association between HCV RNA and LDs was detected in JFH1^{dC3}- or JFH1$^{PP/AA}$-replicating cells (Fig. 2b). Northern blot analysis revealed that 4.8% and 5.4% of total plus- and minus-strand HCV RNA, respectively, were detected in purified LD fractions of JFH^{E2FL}-replicating cells (data not shown). Induction of LD formation with oleic acid did not affect HCV RNA accumulation around LDs (data not shown). These results provide strong evidence that Core recruits HCV RNA as well as NS proteins to LDs.

The HCV replication complex is compartmentalized by lipid bilayer membranes[16–18]. Therefore, HCV RNA in the complex is resistant to nuclease treatment in digitonin-permeabilized cells[17] (Supplementary Information, Fig. S4b–d). *In situ* hybridization analysis did not reveal a significant difference in the number of cells containing LD-associated HCV RNA before and after nuclease treatment (Fig. 2c), indicating that HCV RNA around LDs is part of the replication complex. An RNA synthesis assay showed that the purified LD fraction from JFH1^{E2FL}-, but not JFH1^{dC3}- or JFH1$^{PP/AA}$-replicating cells, possessed HCV RNA synthesis activity, even though the expression levels of viral proteins and RNA-synthesizing activities in total cell lysates were similar (Fig. 2d). Moreover, the addition of Core^{Wt} rescued the localization of plus- and minus-strand

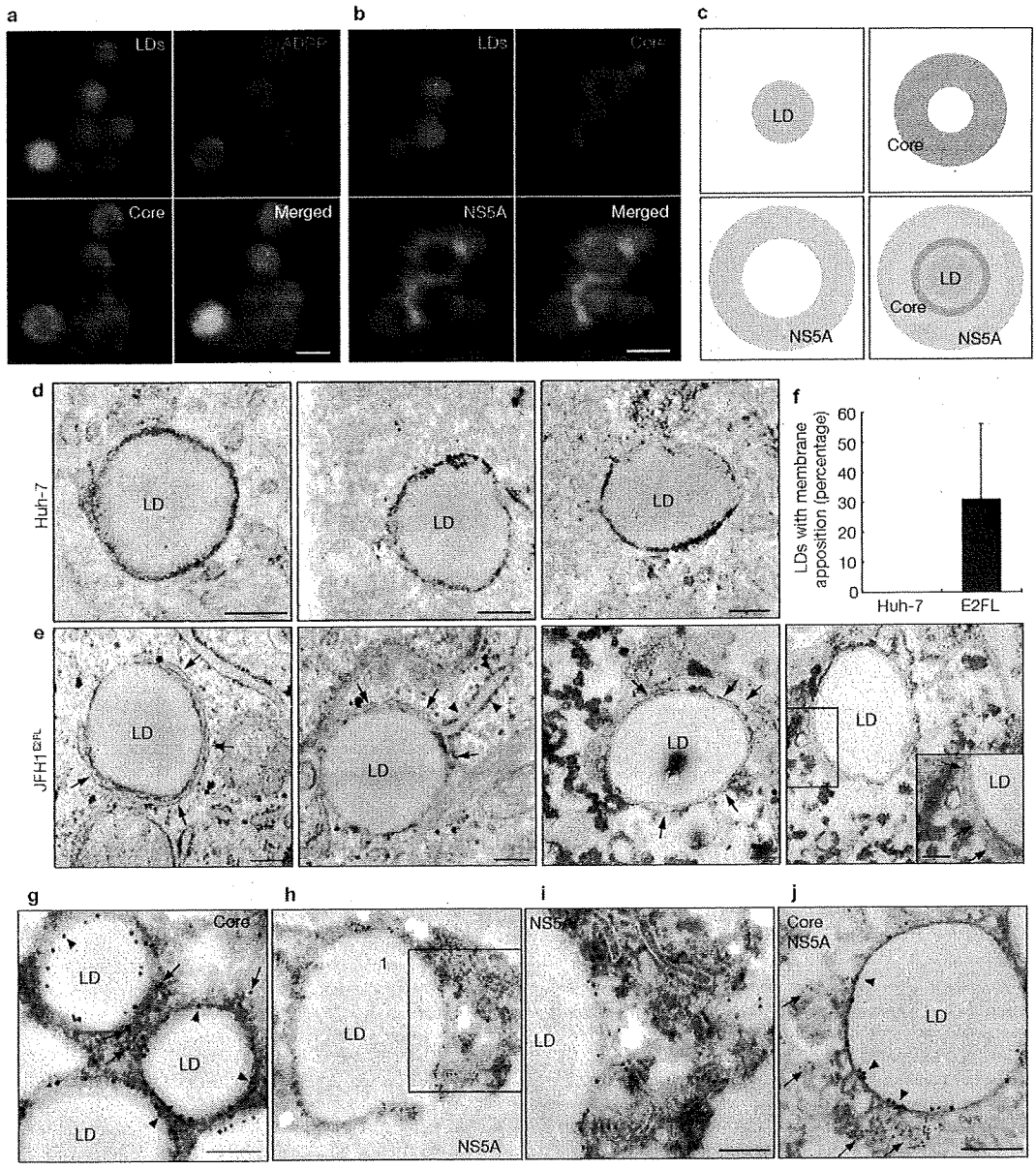

Figure 3 Spatial distribution of Core and NS5A relative to the LD. (**a**, **b**) The localizations of Core, NS5A and ADRP around the lipid droplets (LDs) in JFH1^{E2FL} replicon-bearing cells were analysed using immunofluorescence microscopy. Scale bars, 1 μm. (**c**) Typical images of the localization of LDs, Core, NS5A and merged images are shown with the relative scale of each image. (**d**, **e**) Transmission electron micrographs of LDs in naïve Huh-7 cells and JFH1^{E2FL}-expressing cells. Arrows and arrowheads indicate LD-associated membranes and rough ER membranes, respectively. (**f**) Frequency of LDs with close appositions of membrane cisternae. About 100 Huh-7 cells or JFH1^{E2FL}-expressing cells, respectively, were chosen randomly. LDs with apposed membrane cisternae, as exemplified in panel **e**, were counted as positive. The LDs judged as positive were divided by the total number of LDs. (**g**–**j**) Immunoelectron micrographs of LDs labelled with antibodies against Core (**g**), NS5A (**h**, **i**) or both (**j**) are shown. Panel **i** is a higher magnification of area 1 in panel **h**. In panel **j**, Core and NS5A are labelled with 15 nm and 10 nm gold particles, respectively. Scale bars, 200 nm. All error bars are derived from s.d.

HCV RNA around LDs in JFH^{dC3}-replicating cells (Fig. 2e and data not shown). Both plus- and minus-strand RNA associated with LDs were nuclease resistant (data not shown). These results demonstrate that Core recruits biologically active replication complexes to LDs.

The LD is surrounded by a phospholipid monolayer[19], whereas HCV replication complexes are likely to be surrounded by lipid bilayer membranes[16,17]. Therefore, the replication complexes might not be directly associated with the membranes of LDs. To characterize the colocalization of LDs, viral proteins and replication complexes more precisely, we analysed the localization of NS5A with high-resolution immunofluorescence microscopy. Core was completely colocalized with ADRP, residing on the surface of LDs[20] (Fig. 3a), thus indicating that Core also directly associates with the surface of LDs. More importantly, NS5A mainly localized around the Core-positive area, resulting in a doughnut-shaped signal with a diameter slightly

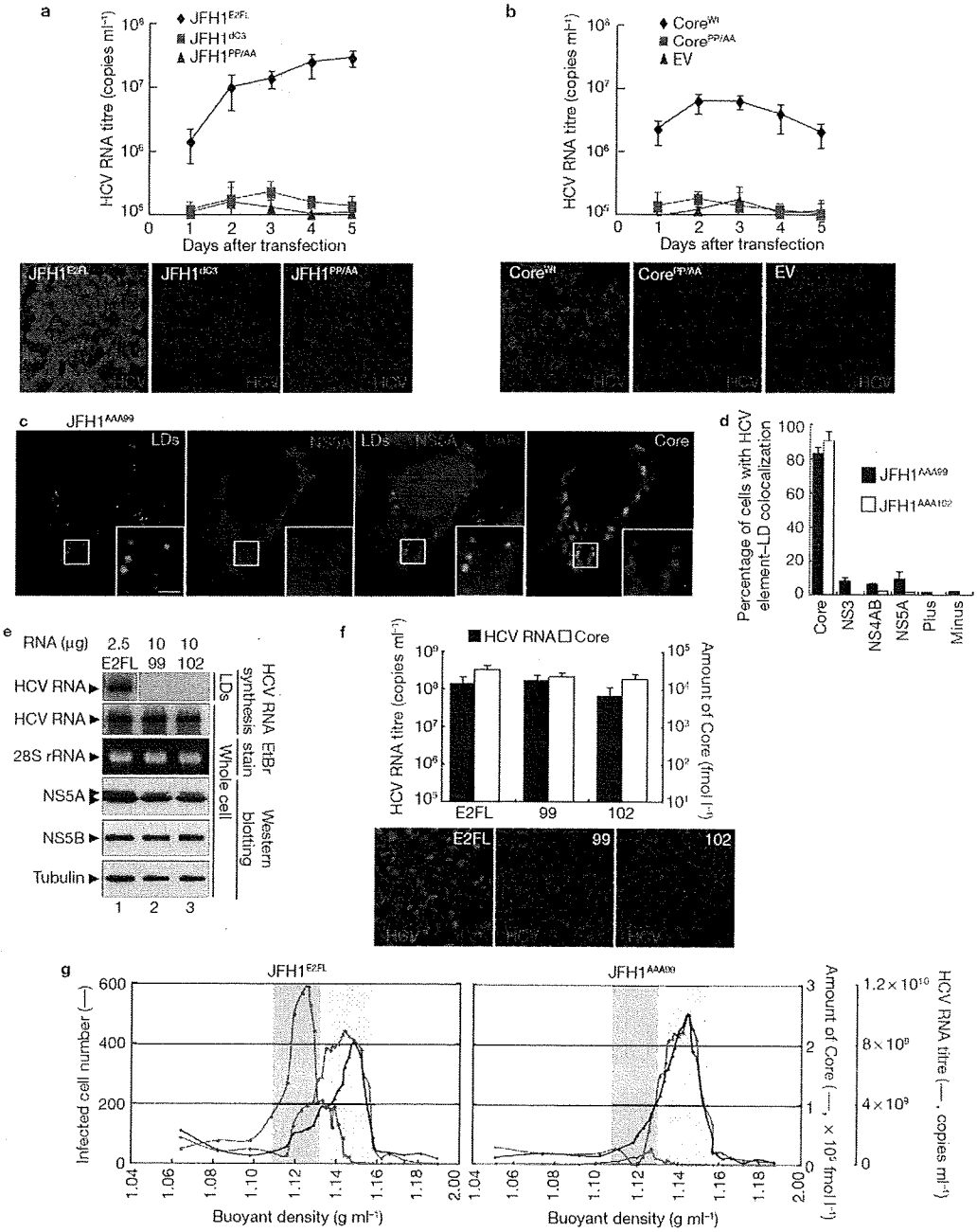

Figure 4 LD associations of Core and NS proteins are necessary for the production of infectious HCV particles. (**a**) The culture medium from JFH1^{E2FL}-, JFH1^{dC3}- or JFH1$^{PP/AA}$-replicating cells was collected at the indicated time points and the titre of hepatitis C virus (HCV) RNA was measured by real-time RT-PCR (upper panel, $n = 3$). The culture medium was added to naïve Huh7.5 cells and, 24 h after inoculation, and cells were labelled with anti-HCV antibodies (lower panels, red). (**b**) JFH1^{dC3} replicon-bearing cells were transfected with pcDNA3 (EV), pcDNA3–Core^{Wt} (Core^{Wt}) or pcDNA3–Core$^{PP/AA}$ (Core$^{PP/AA}$). The level of HCV RNA and the infectivity of the culture medium were examined as described above ($n = 3$). (**c**) Subcellular localization of NS5A and Core in cells expressing JFH1^{AAA99}. The insets are high magnifications of the area of the corresponding panel. Scale bar, 2 μm. (**d**) Percentages of cells in which the signals for given HCV proteins, and plus- and minus-strand HCV RNA, overlapped with those for LDs ($n > 200$). (**e**) Different amounts of JFH1^{E2FL} (E2FL), JFH1^{AAA99} (99) or JFH1^{AAA102} (102) RNAs, respectively, were transfected into the same number of Huh-7 cells. HCV RNA synthesis activity in purified LD fractions (LD) and whole-cell lysates (whole cell) was analysed (HCV RNA synthesis). 28S rRNA was used as a control. Western blot analysis of NS5A, NS5B and tubulin in cells is also shown. All the RNA samples in the top panel were run on the same gel. (**f**) Analysis of HCV released from cells expressing JFH1^{E2FL}, JFH1^{AAA99} or JFH1^{AAA102}. HCV RNA titres (black bars) and amounts of Core (white bars) accumulated in the culture medium at 5 d after RNA transfection were measured (upper panel, $n = 3$). Infectivity of the culture medium for naïve Huh-7.5 cells was analysed as described above (lower panels). (**g**) Concentrated culture medium from JFH1^{E2FL}- and JFH1^{AAA99}-replicating cells was fractionated using 20–50% sucrose density-gradient centrifugation at 100,000 *g* for 16 h. For each fraction, the amounts of Core (black line), HCV RNA (blue line) and infectivity (represented by infected cell numbers in a well; red line) are plotted against the buoyant density (*x*-axis) ($n = 3$). Uncropped images of gels are shown in Supplementary Information Fig. S6. All error bars are derived from s.d.

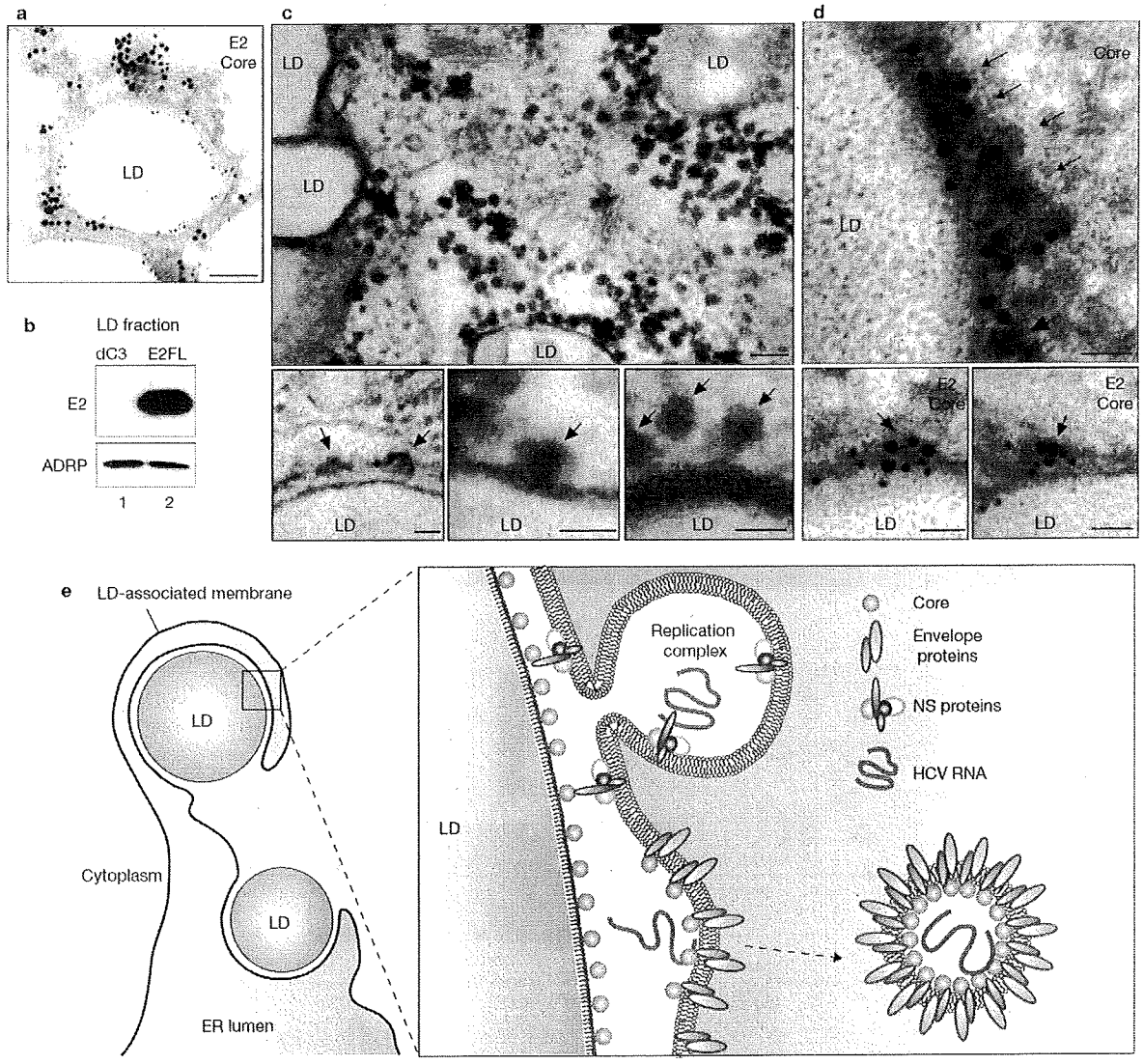

Figure 5 Virus-assembly takes place around the LDs. (**a**) Immunoelectron microscopic detection of E2 and Core in JFH1^{E2FL}-replicating cells. E2 and Core are labelled with 15 nm and 10 nm gold particles, respectively. (**b**) Western blot analysis of the lipid droplet (LD) fraction from JFH1^{E2FL} and JFH1^{dC3} replicon-bearing cells with anti-E2 and anti-ADRP antibodies. (**c**) Transmission electron micrographs of JFH1^{E2FL}-replicating cells. Arrows indicate virus-like particles. (**d**) Immunoelectron micrographs of LDs labelled with antibodies against Core (10 nm) and E2 (15 nm) are shown. Arrows show Core in electron-dense granules. Scale bar: **a** and upper panel of **c**: 100 nm; in **d** and lower panels of **c**: 50 nm. (**e**) A model for the production of infectious hepatitis C virus (HCV). Core mainly localizes on the monolayer membrane that surrounds the LD. HCV induces the apposition of the LD to the endoplasmic reticulum (ER)-derived bilayer membranes (LD-associated membrane). Core recruits NS proteins, as well as replication complexes, to the LD-associated membrane. NS proteins around the LD can then participate in infectious virus production. E2 also localizes around the LD. Through these associations, virion assembly proceeds in this local environment. Uncropped images of gels are shown in Supplementary Information Fig. S6.

larger than that of Core (Fig. 3b). The LD-proximal NS5A signal partially overlapped with the Core signal (Fig. 3b, c, grey). This concentric staining pattern was also observed with the other NS proteins (Supplementary Information, Fig. S5a), indicating that NS proteins associate with Core on the surface of LDs. Electron microscopic analysis only rarely revealed a close association of LDs with other organelles in naïve Huh-7 cells (Fig. 3d, f). However, in the case of JFH1^{E2FL}-replicating cells, about 30% of the LDs were in close proximity to membrane cisternae (Fig. 3e, arrows; 3f), arguing for a HCV-induced membrane rearrangement around LDs. Core was mainly located on the periphery of LDs, and occasionally signals were observed in more distal areas of the LDs (Fig. 3g, arrowheads and arrows, respectively). Although some NS5A signals were observed on the surface of the LD, the majority of NS5A signals were detected more distal of LDs (Fig. 3h, i). Furthermore, we often observed membrane cisternae as white lines in the same area as NS5A signals (Fig. 3i, arrows). When the same section was labelled with anti-Core and anti-NS5A antibodies, Core was detected on the surface of the LDs, whereas NS5A was mainly observed in the peripheral area of the LDs (Fig. 3j, arrowheads and arrows, respectively). In summary, these results show that Core recruits NS proteins, as well as HCV replication complexes, to the LD-associated membranes.

The above results prompted us to ask whether Core–LD colocalization is important for the production of infectious virus particles. JFH1^{E2FL}-replicating cells released virions into the culture medium and these viruses were highly infectious for naïve Huh-7.5 cells[11,21], although culture medium from JFH1$^{pp/AA}$- or JFH1^{dC3}-replicating cells did not contain significant levels of HCV RNA and infectious virus (Fig. 4a). However, following trans-complementation with Core^{Wt}, a high titre of HCV RNA and infectious virus could be rescued from JFH1^{dC3}-replicating cells (Fig. 4b; and see Supplementary Information, Fig. S5b, c). In contrast, the production of infectious viruses was not rescued by trans-complementation with Core$^{pp/AA}$ (Fig. 4b). RNA-binding properties and oligomerization of Core^{Wt} and Core$^{pp/AA}$, which are both necessary for virus assembly, were similar (Supplementary Information, Fig. S5d; ref. 22), arguing that the primary defect of this mutant in preventing infectious virus production is the inability to associate with LDs.

To investigate the contribution of NS proteins around LDs to infectious virus production, we used variants of NS5A, which were not recruited to LDs even in the presence of Core. We assumed that NS5A was crucial for recruiting other NS proteins to LDs, because the level of NS5A recruited to LDs via Core was higher than the levels of the other recruited NS proteins (Fig. 1c, JFH1^{E2FL}). Using alanine-scanning mutagenesis within the NS5A coding region of JFH1^{E2FL}, we generated two mutants, JFH1^{AAA99} and JFH1^{AAA102}, in which the amino-acid sequence APK (aa 99–101 of NS5A) or PPT (aa 102–104 of NS5A) was replaced by AAA (Supplementary Information, Fig. S1). In JFH1^{AAA99}- and JFH1^{AAA102}-replicating cells, NS5A was rarely detected around LDs, whereas Core was still localized to LDs (Fig. 4c, d). Importantly, these mutations impaired not only the NS5A association with LDs, but also the recruitment of other NS proteins and viral RNAs to LDs (Fig. 4d). These results indicate that NS5A is a key protein that recruits replication complexes to LDs. Importantly, HCV RNA synthesis activity in the LD fractions from these mutant JFH1-replicating cells was also severely impaired (Fig. 4e), corroborating the lack of association of HCV replication complexes with LDs.

To investigate the infectious virus production of these NS5A mutants, we prepared cells expressing similar levels of HCV proteins and RNA by adjusting the amount of transfected HCV RNA (Fig. 4e). This was necessary, because replication activities of these mutants were lower compared with JFH1^{E2FL}. Under these conditions, the amounts of Core and HCV RNA that were released into the culture medium from cells transfected with the mutants were comparable to JFH^{E2FL} (Fig. 4f, upper graph). However, infectivity titres of the mutants were severely reduced (Fig. 4f, lower panels). In sucrose density-gradient centrifugation of culture medium from JFH1^{E2FL}-bearing cells, two types of HCV particles were detected: low-density particles (about 1.12 g ml^{-1}) with high infectivity (Fig. 4g, green area of JFH1^{E2FL}), and high-density particles (about 1.15 g ml^{-1}) without infectivity (yellow area). This result indicates that only a minor portion of released HCV particles is infectious, whereas the majority of released particles lack infectivity. In contrast, cells bearing the JFH1^{AAA99} mutant almost exclusively released non-infectious particles of around 1.15 g ml^{-1}, whereas infectious particles were barely detectable (Fig. 4g, JFH1^{AAA99}). Taken together, these results provide convincing evidence that the association of NS proteins and replication complexes around LDs is critical for producing infectious viruses, whereas production of non-infectious viruses seems to follow a different pathway.

The results described so far imply that some step(s) of HCV assembly take place around LDs. To explore this possibility, we analysed the distribution of the major envelope protein E2 around the LD. Electron microscopic analysis revealed that, in about 90% of JFH1^{E2FL}-replicating cells, E2 was localized in the peripheral area of the LDs (Fig. 5a, large grains). This labelling pattern was similar to the one observed for NS5A (Fig. 3j), indicating that E2 also localizes on the LD-associated membranes. Western blot analysis of the LD fraction supported this conclusion, because the LD fraction that was purified from JFH1^{E2FL}-replicating cells, but not from JFH1^{dC3}-replicating cells, contained E2 (Fig. 5b). Furthermore, spherical virus-like particles with an average diameter of about 50 nm were observed around LDs in JFH1^{E2FL}-replicating cells (Fig. 5c, upper panel). These particles were never observed in naïve Huh-7 cells. A more refined analysis indicates that these particles are closely associated with membranes in close proximity to LDs (Fig. 5c, lower panels, arrows). Finally, these particles around the LDs reacted with Core- and E2-specific antibodies, arguing that the particles represent true HCV virions (Fig. 5d). These results suggest that infectious HCV particles are generated from the LD-associated membranous environment.

In this study, we have demonstrated that Core recruits NS proteins, HCV RNAs and the replication complex to LD-associated membranes. Mutations of Core and NS5A (Fig. 4), which failed to associate with LDs, impaired the production of infectious virus. We note that the mutant Core retains the ability to interact with RNA (Supplementary Information, Fig. S5b) and to assemble into nucleocapside[22]. Similarly, the NS5A mutant still supports viral genome replication and the formation of capsids or virus-like particles, arguing that the introduced mutations in Core and NS5A do not affect overall protein folding, stability or function (Fig. 4). Taken together, the data show that the association of HCV proteins with LDs is important for the production of infectious viral particles (Fig. 5e).

Our results also indicate that NS proteins around the LDs participate in the assembly of infectious virus particles. In one scenario, NS proteins may indirectly contribute to the different steps of virus production — for example, by establishing the microenvironment around the LDs that is required for infectious virus production. Alternatively, NS proteins around the LDs may directly participate in virus production — for example, as components of the replication complex that provide the RNA genome to the assembling nucleocapsid.

In support of the role of LDs in virus formation, we observed that colocalization of HCV protein with LDs was low in cases of the chimera Jc1, supporting up to 1,000-fold higher infectivity titres compared with JFH1 (ref. 13). In a Jc1-infected cell, only about 20% of LDs demonstrated detectable colocalization with Core, but this value increased to 80% in the case of a Jc1 mutant lacking most of the envelope glycoprotein genes and thus being unable to produce infectious virus particles (data not shown). This inverse correlation between the efficiency of virus production and Core protein accumulation on LDs indicates that rapid assembly and virus release results in the rapid liberation of HCV proteins from the LDs.

Steatosis and abnormal lipid metabolism caused by chronic HCV infection may be linked to enhanced LD formation[14]. In fact, the overproduction of LDs is induced by Core (Supplementary Information, Fig. S3) and HCV also induces membrane rearrangements around LDs (Fig. 3d–f). Our findings suggest that excessive Core-dependent formation of LDs

and membrane rearrangements are required to supply the necessary microenvironment for virus production. NS proteins and HCV RNA seem to be translocated from the ER to the LD-associated membranes. Interestingly, the LD-associated membranes were occasionally found in continuity with ribosome-studded rough ER (Fig. 3e, arrowheads). Thus, at least parts of the LD-associated membranes are likely to be derived from ER membranes. ER marker proteins, however, were not detected in the LD fraction, suggesting that the LD-associated membrane is characteristically distinct from that of ER membranes.

To our knowledge, this is the first report showing that LDs are required for the formation of infectious virus particles. The fact that capsid protein of the hepatitis G virus also localizes to LDs[15] indicates that LDs might be important for the production of other viruses as well. Our findings demonstrate a novel function of LDs, provide an important step towards elucidating the mechanism of HCV virion production and open new avenues for novel antiviral intervention. □

METHODS

Antibodies. The antibodies used for immunoblotting and immunolabelling were specific for Core (#32-1 and RR8); E2 (AP-33 (ref. 23); 3/11, CBH5 and Flag M2 (Sigma-Aldrich, St Louis, MO); NS3 (R212)[17]; NS4A and 4B (PR12); NS5A (NS5ACL1); NS5B (NS5B-6 and JFH1-1)[24]; ADRP (Progen Biotechnik, Heidelberg, Germany); tubulin (Oncogene Research Products, MA, USA); Grp78 (StressGen, Victoria, Canada); PDI (StressGen); and Calnexin-NT (StressGen). Antibodies specific for Core (#32-1 and RR8), NS3 (R212) and NS4AB (PR12) were gifts from Dr Kohara (The Tokyo Metropolitan Institute of Medical Science, Japan). Anti-E2 antibody (AP-33) was provided by Dr Patel (MRC Virology Unit, UK). Anti-NS5B (NS5B-6) antibody was kindly provided by Dr Fukuya (Osaka University, Japan). Rabbit polyclonal antibodies specific for NS5A were raised against a bacterially expressed GST–NS5A (1–406 aa) fusion protein. In the case of the HCV chimeras Con1/C3 and H77/C3, immunofluorescence analyses were performed by using the following antibodies: Core (C7/50)[5], a JFH1 NS3-specific rabbit polyclonal antiserum; NS4B (#86)[25]; and NS5A (Austral Biologicals, San Ramon, CA).

Indirect immunofluorescence analysis. Indirect immunofluorescence analysis was performed essentially as described previously[17], with slight modifications. Cells transfected with JFH1 RNA were seeded onto a collagen-coated Labtech II 8-well chamber (Nunc, NY, USA). The coating with collagen was performed using rat-tail collagen type I (BD Bioscience, Palo Alto, CA) according to manufacturer's instructions. Three days after seeding, the cells were washed twice with phosphate-buffered saline (PBS; 137 mM NaCl, 2.7 mM KCl, 4.3 mM Na_2HPO_4 and 1.4 mM KH_2PO_4) and fixed with fixation solution (4% paraformaldehyde and 0.15 M sodium cacodylate at pH 7.4) for 15 min at room temperature. After washing with PBS, the cells were permeabilized with 0.05% Triton X-100 in PBS for 15 min at room temperature. For the precise localization of the proteins, the cells were permeabilized with 50 μg ml^{-1} of digitonin in PBS for 5 min at room temperature[26]. After incubating the cells with blocking solution (10% fetal bovine serum and 5% bovine serum albumin (BSA) in PBS) for 30 min, the cells were incubated with the primary antibodies. The fluorescent secondary antibodies were Alexa 568- or Alexa 647-conjugated anti-mouse or anti-rabbit IgG antibodies (Invitrogen, Carlsbad, CA). Nuclei were labelled with 4',6-diamidino-2-phenylindole (DAPI). LDs were visualized with BODIPY 493/503 (Invitrogen). Analyses of JFH1 were performed on a Leica SP2 confocal microscope (Leica, Heidelberg, Germany). Analysis of the Con1/C3 and the H77/C3 chimeras was performed in the same way, except that imaging was performed on a Nikon C1 confocal microscope (Nikon, Tokyo, Japan).

Electron microscopy. For conventional electron microscopy, cells cultured in plastic Petri dishes were processed *in situ*. The cells were fixed in 2.5% glutaraldehyde and 0.1 M sodium phosphate (pH 7.4), and then in OsO_4 and 0.1 M sodium phosphate (pH 7.4). The cells were then dehydrated in a graded ethanol series and embedded in an epoxy resin. Ultrathin sections were cut perpendicular to the base of the dish. For immuno-electron microscopy, cells were detached from the dish with a cell scraper after fixation in 4% paraformaldehyde, 0.1% glutaraldehyde and 0.1 M sodium phosphate (pH 7.4) for 24 h, and washed in 0.1 M lysine, 0.1 M sodium phosphate (pH 7.4) and 0.15 M sodium chloride. After dehydrating the cells in a graded series of cold ethanol, they were embedded in Lowicryl K4M at −20 °C. Ultrathin sections were labelled with primary antibodies and colloidal gold particles (15 nm) conjugated to anti-mouse IgG or anti-rabbit IgG antibodies. For double labelling, colloidal gold particles with different diameters (10 nm and 15 nm) conjugated to anti-mouse IgG or anti-rabbit antibodies were used. Samples were observed after staining with uranyl acetate and lead citrate with a JEM 1010 electron microscope at the accelerating voltage of 80 kV. Anti-Core (#32-1 and RR88), anti-NS5A (NS5ACL1) and anti-E2 (Flag M2) antibodies were used.

Preparation of the lipid droplets. Cells at a confluency of ~80% on a dish with a diameter of 14 cm were scraped in PBS. The cells were pelleted by centrifugation at 1,500 rpm. The pellet was resuspended in 500 μl of hypotonic buffer (50 mM HEPES, 1 mM EDTA and 2 mM $MgCl_2$ at pH 7.4) supplemented with protease inhibitors (Roche Diagnostics, Basel, Switzerland) and was incubated for 10 min at 4 °C. The suspension was homogenized with 30 strokes of a glass Dounce homogenizer using a tight-fitting pestle. Then, 50 μl of 10× sucrose buffer (0.2 M HEPES, 1.2 M KoAc, 40 mM $Mg(oAc)_2$ and 50 mM DTT at pH 7.4) was added to the homogenate. The nuclei were removed by centrifugation at 2,000 rpm for 10 min at 4 °C. The supernatant was collected and centrifuged at 16,000 *g* for 10 min at 4 °C. The supernatant (S16) was mixed with an equal volume of 1.04 M sucrose in isotonic buffer (50 mM HEPES, 100 mM KCl, 2 mM $MgCl_2$ and protease inhibitors). The solution was set at the bottom of 2.2-ml ultracentrifuge tube (Hitachi Koki, Tokyo, Japan). One milliliter of isotonic buffer was loaded onto the sucrose mixture. The tube was centrifuged at 100,000 *g* in an S55S rotor (Hitachi Koki) for 30 min at 4 °C. After the centrifugation, the LD fraction on the top of the gradient solution was recovered in isotonic buffer. The suspension was mixed with 1.04 M sucrose and centrifuged again at 100,000 *g*, as described above, to eliminate possible contamination with other organelles. The collected LD fraction was used for western blotting or the HCV RNA synthesis assay.

HCV RNA synthesis assay. An assay of HCV RNA synthesis using digitonin-permeabilized cells was performed as described previously[17]. For RNA synthesis assays using the LD fraction, the LD fraction collected by sucrose-gradient sedimentation was suspended in buffer B, which contained 2 mM manganese (II) chloride, 1 mg ml^{-1} acetylated BSA (Nacalai Tesque, Kyoto, Japan), 5 mM phosphocreatine (Sigma), 20 units/ml creatine phosphokinase (Sigma), 50 μg ml^{-1} actinomycin D, 500 μM ATP, 500 μM CTP, 500 μM GTP (Roche Diagnostics) and 1.85 MBq of [α-^{32}P] UTP (GE Healthcare, Little Chalfont, UK), and incubated at 27 °C for 4 h. The reaction products were analysed by gel electrophoresis followed by autoradiography.

Note: Supplementary Information is available on the Nature Cell Biology website.

ACKNOWLEDGEMENTS

We thank T. Fujimoto and Y. Ohsaki at Nagoya University for helpful discussions and technical assistance. Y.M. is a recipient of a JSPS fellowship. K.S. is supported by Grants-in-Aid for cancer research and for the second-term comprehensive 10-year strategy for cancer control from the Ministry of Health, Labour and Welfare, as well as by a Grant-in-Aid for Scientific Research on Priority Areas "Integrative Research Toward the Conquest of Cancer" from the Ministry of Education, Culture, Sports, Science and Technology of Japan. T.W. is also supported, in part, by a Grant-in-Aid for Scientific Research from the Japan Society for the Promotion of Science; and by the Research on Health Sciences Focusing on Drug Innovation from the Japan Health Sciences Foundation. R.B. is supported by the Sonderforschungsbereich 638 (Teilprojekt A5) and the Deutsche Forschungsgemeinschaft (BA1505/2-1). M.Z. and R.B. thank the Nikon Imaging Center at the University of Heidelberg for providing access to their confocal fluorescence microscopes and Ulrike Engel for the excellent support.

AUTHOR CONTRIBUTIONS

Y.M. and K.S. planned experiments and analyses. Y.M. was responsible for experiments for Figs 1, 2, 3a–c, 4a–e and 5b. K.A., N.U., electron microscopy; T.H., Fig. 1e; M.Z., R.B., Fig. S2e; and K.S. and K.W., Fig. 4f–g. T.W. provided JFH1 strain. Y.M. and K.S. wrote the manuscript. All authors discussed the results and commented on the manuscript.

COMPETING FINANCIAL INTERESTS

The authors declare no competing financial interests.

Published online at http://www.nature.com/naturecellbiology/
Reprints and permissions information is available online at http://npg.nature.com/reprintsandpermissions/

1. Martin, S. & Parton, R. G. Lipid droplets: a unified view of a dynamic organelle. *Nature Rev. Mol. Cell Biol.* **7**, 373–378 (2006).
2. Blanchette-Mackie, E. J. *et al.* Perilipin is located on the surface layer of intracellular lipid droplets in adipocytes. *J. Lipid Res.* **36**, 1211–1226 (1995).
3. Vock, R. *et al.* Design of the oxygen and substrate pathways. VI. structural basis of intracellular substrate supply to mitochondria in muscle cells. *J. Exp. Biol.* **199**, 1689–1697 (1996).
4. Liang, T. J. *et al.* Viral pathogenesis of hepatocellular carcinoma in the United States. *Hepatology* **18**, 1326–1333 (1993).
5. Moradpour, D., Englert, C., Wakita, T. & Wands, J. R. Characterization of cell lines allowing tightly regulated expression of hepatitis C virus core protein. *Virology* **222**, 51–63 (1996).
6. Deleersnyder, V. *et al.* Formation of native hepatitis C virus glycoprotein complexes. *J. Virol.* **71**, 697–704 (1997).
7. Kato, N. *et al.* Molecular cloning of the human hepatitis C virus genome from Japanese patients with non-A, non-B hepatitis. *Proc. Natl Acad. Sci. USA* **87**, 9524–9528 (1990).
8. Hijikata, M. & Shimotohno, K. [Mechanisms of hepatitis C viral polyprotein processing]. *Uirusu* **43**, 293–298 (1993).
9. Dubuisson, J., Penin, F. & Moradpour, D. Interaction of hepatitis C virus proteins with host cell membranes and lipids. *Trends Cell Biol.* **12**, 517–523 (2002).
10. Wakita, T. *et al.* Production of infectious hepatitis C virus in tissue culture from a cloned viral genome. *Nature Med.* **11**, 791–796 (2005).
11. Lindenbach, B. D. *et al.* Complete replication of hepatitis C virus in cell culture. *Science* **309**, 623–626 (2005).
12. Zhong, J. *et al.* Robust hepatitis C virus infection in vitro. *Proc. Natl Acad. Sci. USA* **102**, 9294–9299 (2005).
13. Pietschmann, T. *et al.* Construction and characterization of infectious intragenotypic and intergenotypic hepatitis C virus chimeras. *Proc. Natl Acad. Sci. USA* **103**, 7408–7413 (2006).
14. Moriya, K. *et al.* Hepatitis C virus core protein induces hepatic steatosis in transgenic mice. *J. Gen. Virol.* **78**, 1527–1531 (1997).
15. Hope, R. G., Murphy, D. J. & McLauchlan, J. The domains required to direct core proteins of hepatitis C virus and GB virus-B to lipid droplets share common features with plant oleosin proteins. *J. Biol. Chem.* **277**, 4261–4270 (2002).
16. Egger, D. *et al.* Expression of hepatitis C virus proteins induces distinct membrane alterations including a candidate viral replication complex. *J. Virol.* **76**, 5974–5984 (2002).
17. Miyanari, Y. *et al.* Hepatitis C virus non-structural proteins in the probable membranous compartment function in viral genome replication. *J. Biol. Chem.* **278**, 50301–50308 (2003).
18. Quinkert, D., Bartenschlager, R. & Lohmann, V. Quantitative analysis of the hepatitis C virus replication complex. *J. Virol.* **79**, 13594–13605 (2005).
19. Tauchi-Sato, K., Ozeki, S., Houjou, T., Taguchi, R. & Fujimoto, T. The surface of lipid droplets is a phospholipid monolayer with a unique fatty acid composition. *J. Biol. Chem.* **277**, 44507–44512 (2002).
20. Londos, C., Brasaemle, D. L., Schultz, C. J., Segrest, J. P. & Kimmel, A. R. Perilipins, ADRP, and other proteins that associate with intracellular neutral lipid droplets in animal cells. *Semin. Cell Dev. Biol.* **10**, 51–58 (1999).
21. Blight, K. J., McKeating, J. A. & Rice, C. M. Highly permissive cell lines for subgenomic and genomic hepatitis C virus RNA replication. *J. Virol.* **76**, 13001–13014 (2002).
22. Klein, K. C., Dellos, S. R. & Lingappa, J. R. Identification of residues in the hepatitis C virus core protein that are critical for capsid assembly in a cell-free system. *J. Virol.* **79**, 6814–6826 (2005).
23. Owsianka, A. *et al.* Monoclonal antibody AP33 defines a broadly neutralizing epitope on the hepatitis C virus E2 envelope glycoprotein. *J Virol* **79**, 11095–11104 (2005).
24. Ishii, N. *et al.* Diverse effects of cyclosporine on hepatitis C virus strain replication. *J. Virol.* **80**, 4510–4520 (2006).
25. Lohmann, V., Korner, F., Herian, U. & Bartenschlager, R. Biochemical properties of hepatitis C virus NS5B RNA-dependent RNA polymerase and identification of amino acid sequence motifs essential for enzymatic activity. *J Virol* **71**, 8416–8428 (1997).
26. Ohsaki, Y., Maeda, T. & Fujimoto, T. Fixation and permeabilization protocol is critical for the immunolabeling of lipid droplet proteins. *Histochem. Cell Biol.* **124**, 445–452 (2005).

nature
cell biology

Supplementary Figures and legends

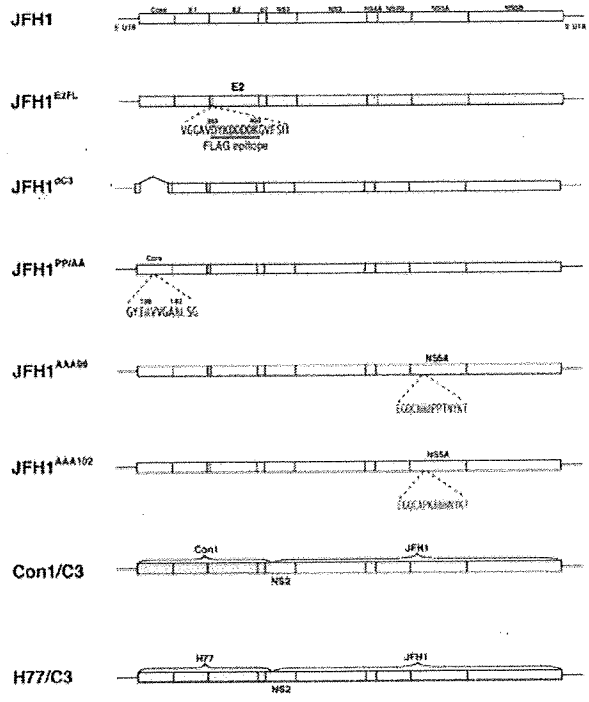

Supplementary Fig. 1

Schematic structures of HCV genomes and mutants used in this study

In JFH1^{E2FL}, the amino acid residues at positions 393 to 400 in the hyper variable region 1 of E2 were converted to a Flag epitope: DYKDDDDK. The JFH1^{E2FL} genome was used to generate other mutant variants of JFH1. In these cases the Flag epitope is marked with a blue vertical line. JFH1^{dC3} carried a deletion in the Core gene that eliminated the 17th to the 163rd amino-acid residue of Core. JFH1$^{PP/AA}$ is a mutant of JFH1^{E2FL} carrying alanine substitutions for proline residues at amino-acid positions 138 and 143 in Core. JFH1^{AAA99} and JFH1^{AAA102} contained mutated NS5A genes carrying triple-alanine substitutions for the APK sequence at amino acid positions 99 to 101 and the PPT sequence at amino acid positions 102 to 104, respectively. Constructs Con1/C3 and H77/C3 are chimeras in which the region from Core to the N-terminal domain of NS2 of JFH1 was replaced by the analogous region of the genotype 1b isolate Con1 or by the genotype 1a isolate H77[6].